

Boosting electrode performance and bubble management via Direct Laser Interference Patterning[†]

Hannes Rox^{*,‡,1,2}, Fabian Ränke^{‡,3}, Jonathan Mädler², Mateusz M. Marzec⁴, Krystian Sokołowski⁴, Robert Baumann³, Homa Hamedi², Xuegeng Yang¹, Gerd Mutschke¹, Leon Urbas², Andrés Fabián Lasagni³, and Kerstin Eckert^{1,2,5}

¹Institute of Fluid Dynamics, Helmholtz-Zentrum Dresden-Rossendorf, 01328 Dresden, Germany. E-mail: h.rox@hzdr.de; k.eckert@hzdr.de

²Institute of Process Engineering and Environmental Technology, Technische Universität Dresden, 01062 Dresden, Germany.

³Institute of Manufacturing Science and Engineering, TU Dresden, 01062 Dresden, Germany.

⁴Academic Centre for Materials and Nanotechnology, AGH University of Krakow, 30-059 Krakow, Poland.

⁵Hydrogen Lab, School of Engineering, Technische Universität Dresden, 01062 Dresden, Germany.

Abstract

Laser-structuring techniques like Direct Laser Interference Patterning show great potential for optimizing electrodes for water electrolysis. Therefore, a systematic experimental study based on statistical design of experiments is performed to analyze the influence of the spatial period and the aspect ratio between spatial period and structure depth on the electrode performance for pure Ni electrodes. The electrochemically active surface area could be increased by a factor of 12 compared to a non-structured electrode. For oxygen evolution reaction, a significantly lower onset potential and overpotential (≈ -164 mV at 100 mA cm^{-2}) is found. This is explained by a lower number of active nucleation sites and, simultaneously, larger detached bubbles, resulting in reduced electrode blocking and thus, lower ohmic resistance. It is found that the spatial distance between the laser-structures is the decisive processing parameter for the improvement of the electrode performance.

*Corresponding author: h.rox@hzdr.de

[†]Electronic Supplementary Information (ESI) available.

[‡]These authors contributed equally to this work.

Broader Context

Central to the efficiency of water electrolysis are gas-evolving electrodes, where the oxygen and hydrogen evolution reaction takes place. However, the gas bubbles evolving cause considerable losses by blocking the electrode surface and increasing the electrolyte resistance and thus, increasing the ohmic losses. Therefore, optimizing the electrode material and surface to manage bubble growth and detachment is a promising approach for enhancing the overall efficiency and cost-effectiveness of water electrolysis. However, it is important that the approach chosen is industrially applicable. Consequently, the focus must be on the utilization of readily available materials, and straightforward and scalable manufacturing techniques. For this reason, nickel was chosen as material as it is widely used in alkaline electrolyzers. By using laser-structuring, a process suitable for industry, the electrode surface can be optimized for water electrolysis to increase the overall efficiency.

1 Introduction

Green hydrogen produced by renewable energies using water electrolysis has become a central technology for the transition towards carbon-neutral industry.^{1,2} Therefore, fossil energies have to be replaced by low or zero-carbon energy sources like solar- or wind-derived electricity to produce hydrogen and replace fossil fuels.^{3,4} This is particularly necessary in end uses that are difficult to electrify, like heavy transport,⁵ maritime applications⁶ or high-temperature processes like steel⁷ or glass industry.⁸

Besides Proton Exchange Membrane (PEM) and Solid Oxide Electrolyzers (SOE), the most mature technology is still alkaline water electrolysis (AWE).⁹ However, large-scale production of green hydrogen still lacks in terms of efficiency, and hence economic competitiveness. Considerable losses are caused by the evolving hydrogen and oxygen bubbles by increasing ohmic resistances and blocking electrochemically active sites.^{10–13} In addition, the mass transfer and the actual current density is influenced by the electrode coverage.^{14–18} These effects can be reduced by applying external forces,^{17,19–24} enhancing bubble coalescence,^{25,26} optimizing the electrode's electrocatalysts,²⁷ morphology^{19,21,28–30} or surface,^{21,31} to achieve an optimized bubble nucleation, growth and detachment.

Knowledge of the forces acting on electrogenerated bubble is crucial here. In general, buoyancy,³² hydrodynamical^{22,32} and Marangoni^{33–35} interfacial tension,^{21,32,36,37} contact pressure³⁷ and electrical forces^{33,38–40} act on an individual bubble. In this study, we focus on the interfacial tension force F_S , given by

$$F_S = -2\pi r_c \gamma \sin\theta, \quad (1)$$

which acts as an retarding force at the three-phase contact line.^{33,36} Here, γ denotes the surface tension. As shown in Eq. 1, besides the contact radius r_c , the contact angle θ has to be taken into account. By changing the wetting behaviour of the surface and thus, increasing or decreasing θ as well as r_c , F_S can be reduced. This results in earlier bubble detachment, thus releasing nucleation sites more quickly and finally increasing efficiency.⁴¹

Electroless deposition,⁴² electrodeposition,^{43–45} lithography,^{46,47} UV lithography³⁰ and laser techniques^{48–53} have recently been reported to optimize the electrode surface. Laser texturing of surfaces offers several advantages, primarily due to its precise control over the size, shape, and distribution of surface features. Laser-based techniques also enable a reproducible process on an industrial scale,⁵⁴ free from chemical reagents and with minimal waste.⁵⁵

Previous studies have demonstrated the use of laser-based methods to create complex patterns on metallic surfaces, featuring repetitive or periodic arrangements. These structures have

been employed to significantly increase electrode surface area, thereby enhancing electrochemical performance of gas evolution reactions.^{48–50} Moreover, when ultrashort laser pulses are applied to metallic surfaces, self-organizing nano- and microstructures are formed, which further increase the electrode surface area and the number of possible nucleation sites. These features, known as Laser-Induced Periodic Surface Structures (LIPSS), arise when materials are irradiated with energy densities near the ablation threshold.^{56–58}

For instance, Direct Laser Writing (DLW) has been used to structure nickel electrodes for applications in electrocatalysis and energy storage.^{59,60} In this context, Rauscher et al. employed a femtosecond pulsed laser to fabricate self-organized conical microstructures on nickel electrodes, achieving a 45 % improvement in Hydrogen Evolution Reaction (HER) efficiency.⁵² However, when features with lateral sizes below a few microns are required, DLW faces limitations in throughput and resolution due to the diffraction limit. A promising alternative capable of overcoming these challenges is Direct Laser Interference Patterning (DLIP). This method, when combined with a high-power picosecond laser source, has been used to create periodic line-like patterns with spatial periods of 11 and 25 μm , improving the efficiency of nickel electrodes for HER up to 22 %.⁴⁸ Additionally, Ränke et al. employed the DLIP technique in conjunction with a femtosecond pulsed laser to generate highly periodic pillar-like patterns with spatial periods of 3 μm , increasing the Electrochemically Active Surface Area (*ECSA*) of nickel-based electrodes by almost 10 times and hence achieving a reduction of overpotential of HER by 49%.⁶¹

As stated above, most reported studies are dealing with HER. However, the exact reaction mechanism and ideal electrodes for the Oxygen Evolution Reaction (OER) are still being researched.⁶² In general, it can be expected that OER requires a higher overpotential to overcome of the kinetic barrier, since it is a four electron-proton coupled reaction compared to the two electron-transfer reaction of HER.⁶³

Therefore, this study systematically investigates the influence of spatial period Λ and structure depth of laser-structured surfaces produced by DLIP on the overall electrode performance during OER. For this purpose, these structures are applied to high-purity Ni as a standard material in alkaline electrolyzers. In addition to surface characterization, the electrochemical performance of the electrodes and the bubble dynamics in terms of detached bubble sizes and number of nucleation sites are analyzed. Using a statistical design of experiment (DoE) approach, models are developed to further optimize the laser structures.

2 Material and methods

Design of Experiments

In order to study the influence of the laser-structuring on the electrode performance, DoE was applied to cover the widest possible range of process parameters and determine the significant structuring parameters.⁶⁴ The design considered three factors: the spatial period Λ , the aspect ratio AR between Λ and structure depth (as shown in Fig. 1), and the current density j . Applying galvanostatic measurement, the influence of these factors on several responses were studied: the quasi-steady state electrode potential E_{SS} , the bubble size (mode (d_m) and median (d_{50}) value of the bubble size distribution), and the mean number of active nucleation centers \bar{n}_{nuc} . Hereby, E_{SS} was defined as the time-averaged potential \bar{E} of the last 20 s of each measurement. Since, nonlinear effects were expected, a full-factorial design on three levels was chosen to study the relationships. The levels are summarized in Tab. 1. A detailed measurement plan is shown in Tab. S1.[†] In order to estimate the measurement noise, the center point was measured independently three times. For better comparison a non-structured reference electrode was studied as well. Thus, $N = 3^3 + 2 + 3 = 32$ experiments were scheduled.

Table 1: Experimental parameters with highlighted center point

Parameter	Range
Spatial period Λ (μm)	6, 15 , 30
Aspect ratio AR (-)	0.33, 0.67 , 1
Current density j (mA cm^{-2})	10, 31.62 , 100

Electrode fabrication

Ni-foils with a thickness of 0.12 mm (GoodFellow, purity 99.95 %) were used as substrate for all electrodes. For better comparison, a non-structured sample (NSE) of the same substrate was cut into the same dimensions of 10 mm \times 50 mm.

The laser texturing was performed by employing an optical configuration with two-beam interference optics. The experimental setup consists of a picosecond solid-state laser (Innoslab PX, EdgeWave, Germany) delivering laser pulses with a pulse duration τ of 12 ps and a maximal average laser power of 60 W. The infrared beam ($\lambda = 1064$ nm) emitted from the laser source is expanded using a two-lens telescope system and guided into the recently developed optical DLIP head (ELIPSYS[®], Surfuntion GmbH, Germany)⁶⁵ that utilizes a Diffractive Optical Element (DOE) to split the incoming main beam into two sub-beams, which later are shaped to elongated lines (see Fig. 1a). The introduced optical head enables an impressive depth of focus of ≈ 10 mm and generates an elliptically shaped laser spot with dimensions ($d_y \times d_x$) of 0.08 mm \times 0.85 mm in the focal plane. Using this optical setup as shown in Fig. 1, considering interference angle θ_{DLIP} as well as the applied laser wavelength λ , the spatial period Λ of the interference pattern can be calculated by

$$\Lambda = \frac{\lambda}{2 \cdot \sin \frac{\theta_{\text{DLIP}}}{2}} \quad (2)$$

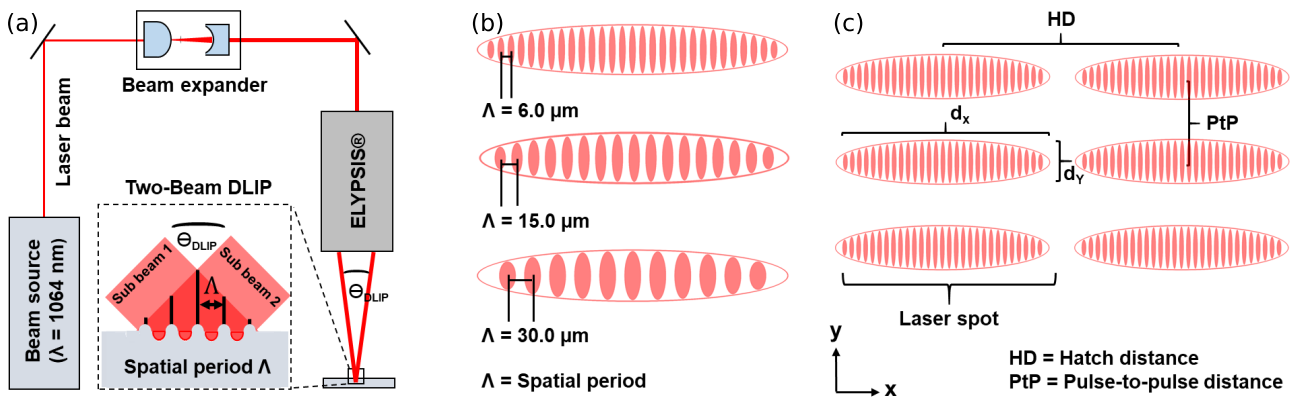


Figure 1: (a) Schematic drawing of the laser texturing showing the two-beam DLIP optical configuration combined with ELIPSYS[®] head. The inset denotes the two overlapping sub-beams producing a line like interference pattern. (b) Resulting interference profiles for spatial periods $\Lambda = 6, 15$ and $30 \mu\text{m}$. (c) Process strategy for structuring surfaces with elongated laser spots and corresponding structure parameter (spot dimensions $d_x = 0.85$ mm, $d_y = 0.08$ mm), pulse-to-pulse distance PtP and hatch distance HD .

For this study the spatial period Λ was changed by swapping the DOE within the optical configuration. The beam splitting mechanism relies on the optical diffraction grating principle, resulting from a periodic structure atop the DOE surface. Depending on the geometric characteristics of the optical grating, the interference angle θ_{DLIP} of the overlapping beams is modified. For the experimental process three distinct DOEs, each corresponding to spatial periods of 6,

15, and 30 μm , were employed. The movement of the metallic substrates in two orthogonal directions was realized with mechanical stages (Aerotech PRO155-05, USA). The texturing was consistently executed at a fixed repetition rate f_{rep} of 10 kHz, using pulse-to-pulse distance PtP of 5 μm (see Fig. 1 (c)). For the treatment of large areas, the hatch distance HD , which is the lateral distance between pulses (see Fig. 1 (c)), was set to 300 μm except for $\Lambda = 6 \mu\text{m}$, where it was adjusted to 360 μm . This increase in HD for the smaller Λ was necessary to prevent partial remelting of the sub-micro textures due to higher localized thermal loads.

Based on a preliminary study (see Sec. S2)[†] on the influence of the number of consecutive passes N on the resulting structure morphology and Aspect Ratio AR , the fabrication of line shaped DLIP features with specific AR of 0.33, 0.67 and 1.0 were conducted by adjusting the number of scans from 1 to 27, utilizing distinct single pulse fluences Φ_{sp} ranging from 0.27 to 0.71 J cm^{-2} . AR is defined to:

$$AR = \frac{\text{Structure depth}}{\Lambda} \quad (3)$$

Experimental methods

A membraneless cell out of PVC (total electrolyte volume $V \approx 60 \text{ mL}$) was used to perform all electrochemical experiments, as shown in Fig. 2. The working electrode (WE) was mounted on an removable holder and pressed between two sheets of compressible PTFE (PTFE.EXS.100, High-tech-flon, Germany) by 10 M4 screws to ensure proper sealing of the active WE area. The open area of the holder was an elongated hole with a diameter of 2 mm and a length of 10 mm (see Fig. S2)[†], which corresponds to an accessible area of the WE of $\approx 0.23 \text{ cm}^2$. The counter electrode (CE) consists out of two pieces of Pt-foil (GoodFellow, purity 99.95 %) with a total area of $A_{\text{el}} \approx 3 \text{ cm}^2$ and was placed horizontally at the top of the cell. A reversible hydrogen reference electrode (Mini RHE, Gaskatel, Germany) was placed inside the cell with tip pointing towards the WE, as it is shown in the highlighted section in Fig. 2. The design of the cell and the WE holder was an adapted version of the cell setup used in Rox et al.⁶⁶ This cell was used for cyclic voltammetry (CV), linear sweep voltammetry (LSV) and galvanostatic measurements.

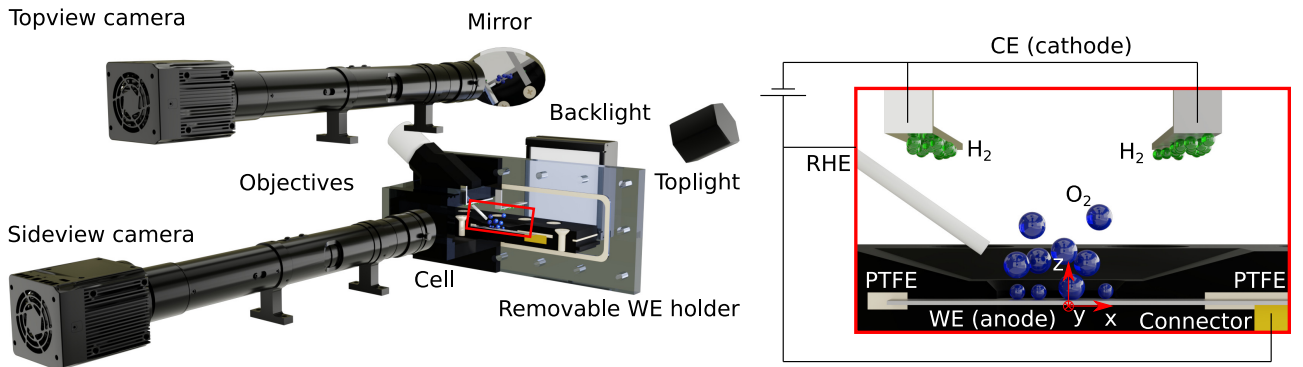


Figure 2: Schematic drawing of the membraneless cell and the optical measurement system used to perform electrochemical measurements and simultaneously study the O_2 bubble evolution.

All experiments were carried out in a 1 M KOH (Titripur, Merck, Germany) solution under ambient conditions ($T = 293 \text{ K}$, $p = 1 \text{ bar}$). Prior to the experiments, the electrolyte was purged with N_2 for 20 min and pumped into the cell under a N_2 atmosphere by means of a OB1 MK3+ (Elveflow, France). All WEs were cleaned in a ultrasonic bath with Isopropanol for 5 min, rinsed with deionized (DI) water and stored in DI water for at least 48 h to ensure a superhydrophilic

surface.⁶⁷ This was proven using a contact angle measurement system (OCA 200, DataPhysics Instruments GmbH, Germany) by applying a water droplet with a volume of 5 μL on the surface, which spreaded directly over the entire structured area.[†] For this purpose, the samples were dried with compressed air before the measurements. Before each measurement performed in the electrochemical cell, the WE was cleaned with ethanol and subsequently rinsed with DI water to remove any remaining contamination before mounting them onto the electrode holder.

Characterization of electrode surfaces.

For evaluating the surface topography of the laser structured samples, White Light Interferometric (WLI) images (Sensofar S-Neox, Spain) were recorded by employing 50x magnification objective. The surface profiles and average structure depth values were obtained using the SensoMAP Advanced Analysis Software (Sensofar, Spain). In addition, high resolution images of the treated substrates were taken using Scanning Electron Microscopy (SEM) operating at an acceleration voltage of 12 kV (Quattro ESEM, Thermo Fischer Scientific, Germany).

X-ray photoelectron spectroscopy (XPS) measurements were performed to characterize the surface composition. Therefore, monochromatic Al $K\alpha$ (1486.6 eV) X-rays were focused to a 100 μm spot using a PHI VersaProbeII Scanning XPS system (ULVAC-PHI). The photoelectron takeoff angle was 45° and the pass energy in the analyzer was set to 117.50 eV (0.5 eV step) for survey scans and 46.95 eV (0.1 eV step) to obtain high energy resolution spectra for the C 1s, O 1s, N 1s, P 2p, S 2p and Ni 2p regions. A dual beam charge compensation with 7 eV Ar⁺ ions and 1 eV electrons was used to maintain a constant sample surface potential regardless of the sample conductivity. All XPS spectra were charge referenced to the unfunctionalized, saturated carbon (C-C) C 1s peak at 285.0 eV. The operating pressure in the analytical chamber was less than 3×10^{-9} mbar. Deconvolution of spectra was carried out using PHI MultiPak software (v.9.9.3).[†] Spectrum background was subtracted using the Shirley method. Details about the deconvolution and fitting of the XPS spectra can be found in Sec. S8.[†] In addition, for individual electrodes detailed XPS measurements were performed to differentiate between bright and dark areas caused by *HD* of the laser-structuring. Therefore, three bright (b1, b2, b3) and three dark (d1, d2, d3) areas were analyzed on each sample.

Characterization of the electrode performance.

Prior to all electrochemical measurements, each electrode was activated by ensuring a constant open circuit potential (OCP) over 5 min and afterwards running 200 cycle voltammograms (CV) at a scan rate of $\nu = 500 \text{ mV s}^{-1}$ from 0.2 V to 1 V vs. RHE. These CVs were also used to specify the potential region where non-Faradaic currents occur to run series of CVs in a range of $\pm 50 \text{ mV}$ around a starting potential within this region. In total 14 different ν (0.02, 0.04, 0.06, 0.08, 0.1, 0.2, 0.3, 0.4, 0.5, 0.6, 0.7, 0.8, 0.9 and 1 V s^{-1}) were applied and for each ν five cycles were performed with a 1 min break after each set. For the calculation of the double-layer capacitance C_{dl} the last three measurements were taken. Linear sweep voltammetry (LSV) was used to calculate the onset potential E_{on} of the OER. A potential range from 0 V to 2.5 V vs. RHE at a scan rate of 100 mV s^{-1} was selected for this purpose. Finally, galvanostatic measurements at fixed current densities (10, 31.62 and 100 mA cm^{-2}) according to Tab. S1[†] were performed over a time of $t = 1 \text{ min}$. Therefore, the applied current was calculated for all electrodes by using the open area of the electrode holder of 0.23142 cm^2 . For all electrochemical measurements a Modulab Xm with a Pstat 1MS/s module (Solartron analytical, Ametek, USA) was used as electrochemical workstation.

Characterization of the bubble evolution.

During the galvanostatic measurements the bubble evolution and detachment were optically investigated from two perspectives (see Fig. 2). Therefore, two high-speed cameras (1920×760 px, IDT OS-7 S3, USA) were used, each equipped with a precision micro-imaging lens with a magnification of 2 and a 12.5:1 zoom-module (Optem® FUSION, USA). This resulted in a resolution of $867.38 \text{ px mm}^{-1}$ and $543.124 \text{ px mm}^{-1}$ for sideview and topview, respectively. The depth of field was determined to be $335 \text{ }\mu\text{m}$ using a calibration plate. A LED-panel (CCS TH2, Japan) as back illumination completed the shadowgraphy measurement system, while the top view was lit at an angle of $\approx 60^\circ$ by a M-LED 3000 plus (ILO electronic, Germany). The field of view (FOV) for the sideview was adjusted right above the electrode cover, to prevent detached bubbles from dissolving, at a sample rate of 250 Hz. To capture the bubble growth the sample rate for topview images was set to 1000 Hz and the FOV was centered in the middle of the xy -plane of the WE surface.

The grayscale images, taken with a 12-bit depth, were analyzed using Python 3.9. The image processing followed the segmentation method introduced in Rox et al..⁶⁶ Thus, a machine-learning (ML) based approach was chosen to segment the bubbles in both sideview and topview. Therefore, for each camera perspective a stardist model (v.0.8.5)^{68,69} was trained with a randomly chosen set of 240 and 100 manual labelled images for sideview and topview, respectively. After segmentation of the detached bubbles in the sideview images, all objects were linked using trackpy⁷⁰ and finally, blurred bubbles were eliminated by calculating the size-normalized variance of the image Laplacian ($\text{Var}(\Delta) \cdot d_B$). Therefore, all segmented bubbles below the 50 % quantile of this metric were excluded from further analysis, as they correspond to the most blurred bubbles.^{43,66} For the topview evaluation, the number of detected bubbles were taken as measure of the active nucleation centers. The stardist model was trained to differentiate between bubbles sitting on the electrode and already detached bubbles by means of the shadow of the inclined illumination. Examples for the image processing steps are shown in Fig. S3 and Fig. S4.[†] All processed data including all relevant metadata is available at [10.14278/rodare.3064](https://doi.org/10.14278/rodare.3064).[†]

Multiple Regression Analysis.

For the multiple regression analysis, the factors (Λ , AR and j) were transformed into the space between -1 and 1. Therefore, the transformation rules shown in Tab. 2 were applied to convert the factors from the real experiment to values between -1 and 1. Afterwards, a response surface model with

$$y = \beta_0 + \beta_1 \bar{\Lambda} + \beta_2 \bar{AR} + \beta_3 \bar{j} + \beta_{12} \bar{\Lambda} \bar{AR} + \beta_{13} \bar{\Lambda} \bar{j} + \beta_{23} \bar{AR} \bar{j} + \beta_{11} \bar{\Lambda}^2 + \beta_{22} \bar{AR}^2 + \beta_{33} \bar{j}^2 \quad (4)$$

was fitted for each response y (see Eq. 4), where y refers to E_{SS} , d_m , d_{50} and \bar{n}_{nucl} . Then, the response surface model was reduced applying backward elimination discarding the least relevant factors (threshold: p-Value > 0.05). Thus, at the end a reduced model for each response was derived.

Due to high number of scans needed for the electrode with $\Lambda = 30 \text{ }\mu\text{m}$ and $AR = 1.0$ and thus, excessive fluence Φ for the given thickness of the substrate, this structure could not be produced reproducibly.[†] Therefore, all measurement points with $\Lambda = 30 \text{ }\mu\text{m}$ and $AR = 1.0$ were neglected in this study and N was reduced by 3. Thus, all developed models can only provide a first approximation since this corner point of the full-factorial design is missing.

3 Results and discussion

Characterization of the electrode structure

As reported in [Heinrich et al.](#), by storing the DLIP-structures in DI water the adsorption of organic compounds is limited and thus, the wettability is increased.⁶⁷ The hydrophilicity of the DLIP-structures and their surface chemistry⁷¹ is supported by the capillary effects of the channels. In comparison to the non-structured electrode (NSE), with a measured static water contact angle (WCA) of $\theta_{\text{NSE}} = 38.5^\circ \pm 2.6^\circ$, WCA measurements were not possible for the superhydrophilic DLIP-structures, since the applied droplets spread directly across the entire electrode surface, as it is shown in Fig. S7.[†] Thus, for all DLIP-structures it can be stated that $\theta \ll \theta_{\text{NSE}}$.

Exemplary confocal microscopic images of the DLIP line-like features with an $AR = 0.67$ are shown in Fig. 3 (a) revealing that with increasing spatial period Λ the structure regularity is decreasing. In this context, the number of applied scans N is the decisive factor, which, as indicated in Fig. 3 (a), was significantly higher for larger structure periods. Generally, the structure formation process was characterized not only by the ablation of the nickel substrate, but also by the redeposition of removed material from the ablation plume.⁷² The amount of redeposited material grows continuously with the increasing number of over scans and therefore had a stronger influence on the regularity of the line-like pattern with $\Lambda = 15$ and $30 \mu\text{m}$. Furthermore, the redeposition occurred predominantly in the areas of interference minima and did not happen uniformly over the whole surface, leading to the formation of a more irregular DLIP texture. This could also be concluded from the plotted height profiles in Fig. 3 (b), in which, e.g., electrode #9 shows a cut-off peak in the structure.

However, as expected the average surface roughness S_a followed a linear trend with Λ (see Fig. 3 (c)). In contrast, the developed interfacial area ratio S_{dr} , as a measure of the additional surface area created by the texture compared to the ideal flat substrate, showed a maximum at $\Lambda = 15 \mu\text{m}$ with an enlargement of $\approx 150 \%$. The complete confocal images of all DLIP-structures can be found in Fig. S5.[†]

For a more detailed analysis of the surface topographies generated, SEM images were recorded. The line-like DLIP patterns for different AR are shown in Fig. 4. The patterns displayed in Fig. 4 (a-c) depict DLIP structures fabricated with $\Lambda = 6 \mu\text{m}$, whereas those in (d-f) exhibit $\Lambda = 15 \mu\text{m}$ and (g-h) present $\Lambda = 30 \mu\text{m}$. The resulting cumulated fluence Φ_{cum} , the number of scans N , as well as AR are given in the labels for each display.

For the samples exhibiting an aspect ratio $AR = 0.33$ the appearance of a homogeneous line-like DLIP pattern decorated with a sub-structure could be observed for all spatial periods.

Table 2: Transformation rules for the multiple regression analysis to scale the factors from the real experiment to values between -1 and 1)

Parameter	Rule
Spatial period Λ	$\bar{\Lambda} = \frac{1}{0.5108} \ln \left(\frac{\frac{\Lambda}{\mu\text{m}} + 7.5}{22.5} \right)$
Aspect ratio AR	$\bar{AR} = \frac{2(AR - \frac{1}{3})}{1 - \frac{1}{3}} - 1$
Current density j	$\bar{j} = \frac{1}{1.151} \cdot \ln \left(\frac{j}{\frac{\text{mA}/\text{cm}^2}{31.62}} \right)$

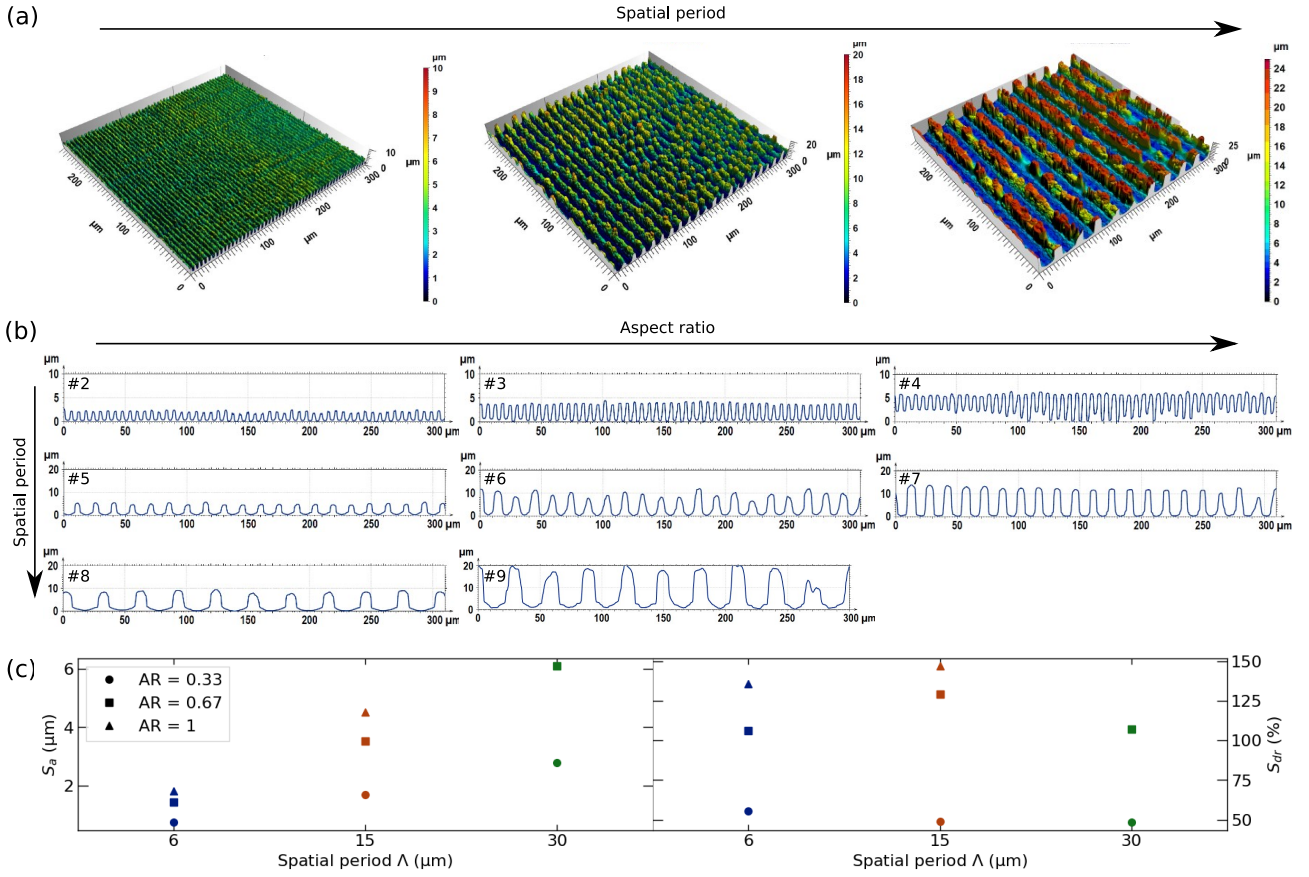


Figure 3: (a) 3D confocal images of DLIP line-like structures with $\Lambda = 6, 15$ and $30 \mu\text{m}$ at $AR = 0.67$. (b) Height profiles of structured Ni-surfaces for all studied electrodes ($\Lambda = 6, 15$ and $30 \mu\text{m}$ and $AR = 0.33, 0.67$ and 1.00). The electrode ID (see Tab. 3) is provided in the upper left corner. (c) Average surface roughness S_a and developed interfacial area ratio S_{dr} as a function of Λ and AR .

Upon inspecting the samples structured with $\Lambda = 6 \mu\text{m}$ (Fig. 4 (a)), $15 \mu\text{m}$ (Fig. 4 (d)) and $30 \mu\text{m}$ (Fig. 4 (g)) at a higher magnification (see insets), the presence of a wavy texture could be observed. For the line texture with $\Lambda = 6 \mu\text{m}$, all areas of the microstructure shown in Fig. 4 (a) were completely covered with the wavy sub-textures. In contrast, for the larger structure periods, ripple textures only occurred in the regions corresponding to the interference maxima positions. However, these ripples were oriented perpendicular to the polarization of the applied laser radiation (double arrow E in Fig. 4 (a)) and cross the generated DLIP lines pattern at an angle of 90° . The measured periodicity of the ripples Λ_{LIPSS} ranged from 740 nm to 930 nm , which corresponds to $70\% - 87\%$ of the used laser wavelength ($\lambda = 1064 \text{ nm}$). These characteristics suggested that the sub-structure can be regarded as LIPSS and further classified as Low-Spatial Frequency LIPSS (LSFL), according to previous studies.⁷³⁻⁷⁵ Furthermore, the linear textures with Λ equal to 15 and $30 \mu\text{m}$, displayed the redeposition of ablated material in the region of minima interference. Apart from this, the formation of microcracks along the structural peaks of DLIP structure became visible for both cases (see Fig. 4 (d) and (g)).

An increase in AR to 0.67 led to the homogenization of the DLIP patterns for the $6 \mu\text{m}$ period, causing the previously visible LSFL substructures to disappear. The redeposition of material in form of nano- and micro particles from the ablation plume was also observed on the structural peaks (Fig. 4 (b)).

The resulting DLIP line patterns with an AR of 0.67 , which are shown in Fig. 4 (e) and (h), were characterized by the formation of a partially irregular DLIP texture, with increased

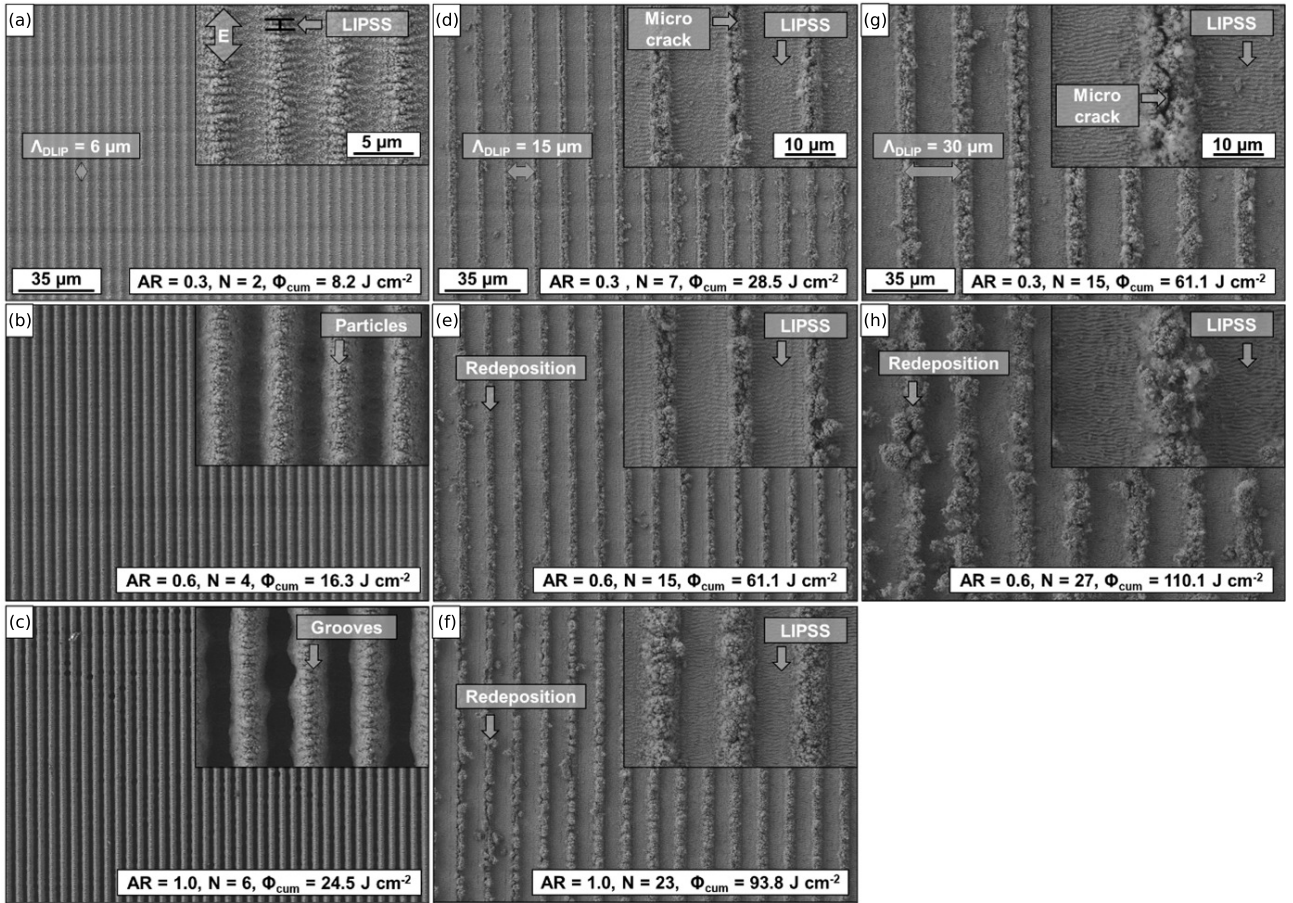


Figure 4: SEM images of DLIP line-like with a spatial period Λ of 6 μm (a,b,c), 15 μm (d,e,f) and 30 μm (g,h) fabricated on nickel foils with a single pulse fluence (Φ_{sp}) of 0.25 J cm^{-2} and a pulse-to-pulse distance (PtP) of 5 μm . The generated aspect ratio AR , the total number of applied passes N and cumulated fluence Φ_{cum} are displayed in the corresponding labels. The scale bars in the first row are representative of all columns.

redeposition of material in the areas of the interference minima. The degree of redeposition was directly dependent on the number of consecutive scans N . For instance, processing with a cumulative fluence Φ_{cum} of 110.1 J cm^{-2} , resulting from 27 consecutive passes in Fig. 4 (h), led to the continuous growth of redeposition clusters, which started to partially shield the areas of the interference maxima. In general, the homogeneity of the surface structures with an AR of 0.67 was observed to steadily decrease with increasing spatial period. Upon closer inspection of the magnified SEM sections for the 15 μm and 30 μm periods, it was apparent that LIPSS textures were still present in the areas of maxima interference.

The deepest line structures were fabricated for $AR = 1$. The SEM images of the resulting line pattern with $\Lambda = 6 \mu\text{m}$ continued to show a high degree of homogeneity. Though it became evident that 6 successive passes had influenced the geometric shape of the individual DLIP features. As a result, the borders between interference maxima and minima developed a wavy characteristic and partially even hole-like structures were formed (Fig. 4 (c) and S6 (b)).^{76,†} For $\Lambda = 15 \mu\text{m}$ in Fig. 4 (f), 23 over scans resulted in a higher amount of redeposited material, leading to an enlargement of line-like DLIP features.

The XPS results in Fig. S10 and Tab. S2[†] show the relative, chemical composition of the electrode samples. The chemical states and surface concentrations of C, O, and Ni were deconvoluted by fitting the XPS spectra. No clear tendency of the influence of Λ and AR was found for the surface composition. With the exception of the group of aliphatic carbon C–C at a binding energy of 285 eV only little differences were found and thus, the further discussion

is focused on electrochemical properties.

Electrochemical characterization of the electrodes

For further characterization of the DLIP-structures, C_{dl} as a measure of *ECSA* was analyzed. C_{dl} was calculated as the slope of the linear fits, shown in Fig. 5 (a) using

$$C_{\text{dl}} = \frac{\bar{I}_{\text{anodic}} + |\bar{I}_{\text{cathodic}}|}{2 \cdot \nu}. \quad (5)$$

By running multiple CVs at different ν (see Fig. S8)[†], the average currents \bar{I} of the last three cycles could be plotted against ν , revealing the linear correlation. In addition to the definition of an unique electrode ID for further discussion of the results, the obtained electrode performance metrics can be found in Tab. 3.

Table 3: Average surface roughness S_a (CM), double-layer capacitance C_{dl} (CV) and onset potential E_{on} (LSV) of all electrodes – Standard deviation was calculated for middle and reference point of DoE

ID	Λ (μm)	AR (-)	S_a (μm)	C_{dl} (μF)	E_{on} (V)
#1	NSE			23.73 ± 1.72	1.743 ± 0.021
#2	6	0.33	0.749	123.50	1.704
#3	6	0.67	1.43	159.26	1.710
#4	6	1	1.83	213.94	1.664
#5	15	0.33	1.70	280.48	1.670
#6	15	0.67	3.53	146.61 ± 4.70	1.690 ± 0.005
#7	15	1	4.53	220.74	1.687
#8	30	0.33	2.80	92.76	1.717
#9	30	0.67	6.10	133.64	1.707

The shown increase of C_{dl} can be attributed to the increase of the developed interfacial area ratio S_{dr} , since the normalized C_{dl} in Fig. 5 (b) follows a similar trend like S_{dr} in Fig. 3 (c) with a maximum at $\Lambda = 15 \mu\text{m}$. In addition, when electrode #5 was neglected, the tendency was found that an increasing *AR* leads to a higher C_{dl} . This also clearly follows the geometric surface enlargement in terms of S_a and S_{dr} . However, at low *AR* and $\Lambda = 15 \mu\text{m}$ or $30 \mu\text{m}$, LSFL were detected in the SEM images, as shown in Fig. 4, which contributed to the increased C_{dl} . In general, it was found that the applied DLIP structuring results in a significant, up to $\approx 12\times$ increase of C_{dl} , which exceeds the increase of C_{dl} achieved by laser-structuring in [Bernäcker et al.](#) and [Baumann et al.](#). However, [Bernäcker et al.](#) used short pulse laser-structuring with non-regular laser structures⁷⁷ and [Baumann et al.](#) used DLIP structuring at a lower spatial period of $\Lambda = 5.8 \mu\text{m}$.⁵⁰

This improvement was also evident in the measured onset potential E_{on} . For this purpose, the intersection of the non-Faradaic and Faradaic current regions of the recorded LSV curves was defined as E_{on} , as shown in Fig. S9[†]. For better comparability, the efficiency η_{on} was defined as

$$\eta_{\text{on}} = \frac{E_{\text{on}} - E_{\text{on, NSE}}}{E_{\text{on, NSE}}}. \quad (6)$$

As a result, it was possible to deduce that the DLIP-structures lead to a reduction of E_{on} up to $\approx 4.5 \%$.

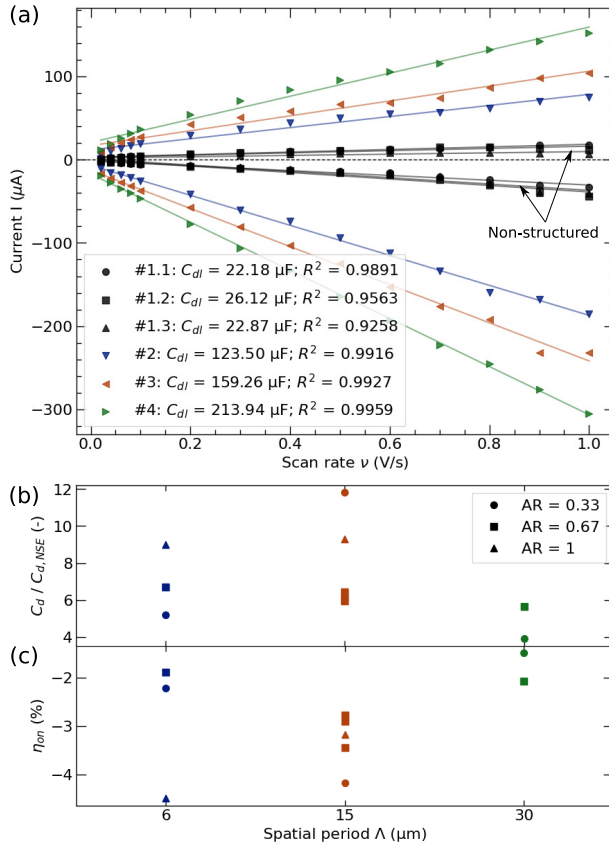


Figure 5: (a) Linear fit of the average anodic and cathodic currents I over ν measured during CV and calculated C_{dl} equal to the slope of the fit for a period length of $6 \mu\text{m}$ at different aspect ratios. (b) Normalized C_{dl} and (c) onset potential η_{on} (see Eq. 6) for all studied electrodes.

In addition, it was found that the laser-structuring has good reproducibility, as can be seen from the data points at $\Lambda = 15 \mu\text{m}$ and $AR = 0.67$ in Fig. 5 (b) and (c) or the calculated standard deviations σ for the middle point of the DoE in Tab. 3 and Tab. S3.[†]

For further characterization of the electrode performance, galvanostatic measurements were run over a time of $t = 60 \text{ s}$ at three different current densities of $j = 10, 31.62$ and 100 mA cm^{-2} . According to Faraday's law

$$I = zFN \quad (7)$$

and assuming equal electrical contact resistances for all measurements, the molar flux of produced O_2 \dot{N}_{O_2} for all measurements at the same current density is constant:

$$\dot{N}_{\text{O}_2}(I) = \text{const.} \quad (8)$$

Since the CE had an area $\approx 12\times$ larger than the WE, it was ensured that the HER is not limiting the OER at the WE. Thus, a change in the measured potential E of the WE could be directly linked to the anodic overpotential η_{anode} and the ohmic overpotential losses η_{Ω} . As a result, a lower measured E leads to a decrease of the cell potential E_{cell} as an important measure of the overall efficiency of water electrolysis,⁷⁸ which is defined as

$$E_{\text{cell}} = |\Delta E^0| + \eta_{\text{anode}} + |\eta_{\text{cathode}}| + \eta_{\Omega} + \eta_{\text{conc.}} \quad (9)$$

As all measurements were carried out in 1 M KOH, the concentration overpotential η_{conc} is negligible.⁷⁸

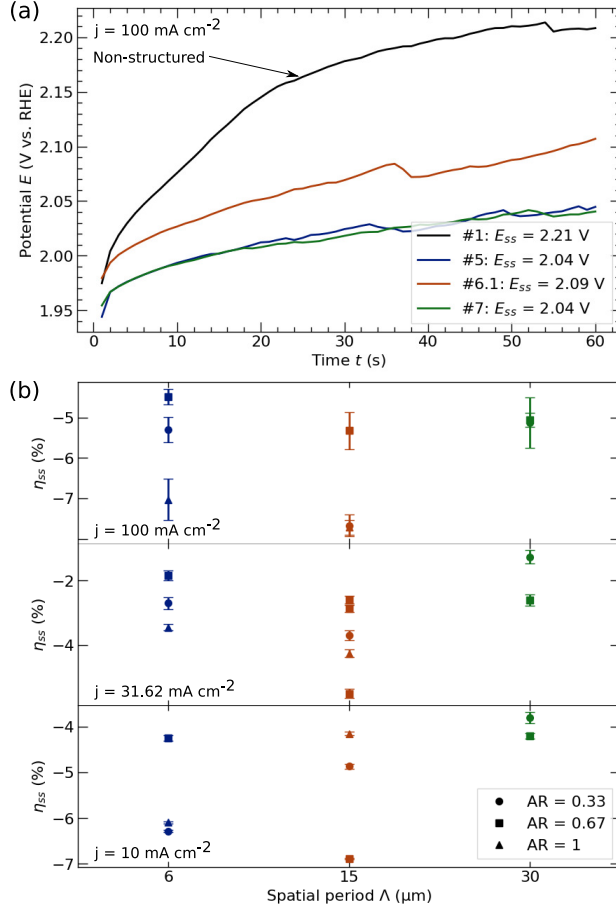


Figure 6: (a) Potential during 60 s galvanostatic measurements for a period length of $6 \mu\text{m}$ at different aspect ratios. (b) Normalized WE overpotential η_{SS} (see Eq. 10) calculated from the quasi-steady state electrode potential E_{SS} at $j = 10, 31.62$ and 100 mA cm^{-2} .

Similar to Eq. 6, the efficiency η_{SS} was defined for better comparability of the quasi-steady state potential E_{SS} :

$$\eta_{SS}(j) = \frac{E_{SS}(j) - E_{SS, \text{NSE}}(j)}{E_{SS, \text{NSE}}(j)} \quad (10)$$

As shown in Fig. 6 E_{SS} was significantly lower for all studied DLIP-structures. The best-performing electrode #7 achieved a $\approx 164 \text{ mV}$ lower E_{SS} at $j = 100 \text{ mA cm}^{-2}$ with electrode #5 performing similarly well, as can be seen in Fig. 6 (a). In addition, the calculated measurement noise of $\sigma \approx 0.024 \text{ V}^\dagger$ served to indicate excellent reproducibility of the DLIP-structuring. It should be emphasized that in Fig. 6 (b) η_{SS} follows a similar trend with a maximum at $\Lambda = 15 \mu\text{m}$ like the normalized C_{dl} in Fig. 5 (b). Since no clear influence on η_{SS} can be identified for AR , the hypothesis can be made that Λ is the decisive factor for DLIP-structuring.

This was also confirmed on the basis of the multiple regression analysis.[†] The obtained model ($R^2 = 0.984$) showed a non-surprising significant influence of j . More interesting was the significance of the influence of Λ on E_{SS} which is confirmed by the significant (thus not eliminated) linear term $\bar{\Lambda}$ and quadratic term for $\bar{\Lambda}^2$ in Eq. 11.

$$E_{SS} = 1.7927 + 0.0074 \bar{\Lambda} + 0.191 \bar{j} + 0.0221 \bar{\Lambda}^2 + 0.0672 \bar{j}^2 \quad (11)$$

The shown improvement of η_{SS} of $\approx -7.7\%$ can be explained by the smaller effective current density j_{eff} due to increased C_{dl} and following, $ECSA$. At $\dot{N}_{\text{O}_2}(I) = \text{const.}$ this leads to decreased η_{Ω} , since more electrode surface is available for the electrode-electrolyte interface.

Detached bubble sizes

For a better understanding of the described improvement of the electrochemical performance of the DLIP-structures, high-speed images of the bubbles were taken. An example of these images with segmented bubbles using the ML-based image analysis is shown in Fig. 7 (a). It should be pointed out that only sharp bubbles inside the focal plane were included in the further evaluation. As the critical KOH concentration for bubble coalescence of 0.053 M ⁷⁹ is clearly exceeded with $c_{\text{KOH}} = 1 \text{ M}$ used, bubble coalescence is suppressed. In addition, as the FOV was placed right above the electrode cover, it could be assumed that the bubble diameters d_B in Fig. 7 (b) correspond to d_B at detachment of the electrode surface. With the measured noise of $\sigma = 17.08 \mu\text{m}$ for d_m and $\sigma = 19.32 \mu\text{m}$ for d_{50} (see Tab. S3)[†], the DLIP-structuring also showed good reproducibility in terms of bubble development.

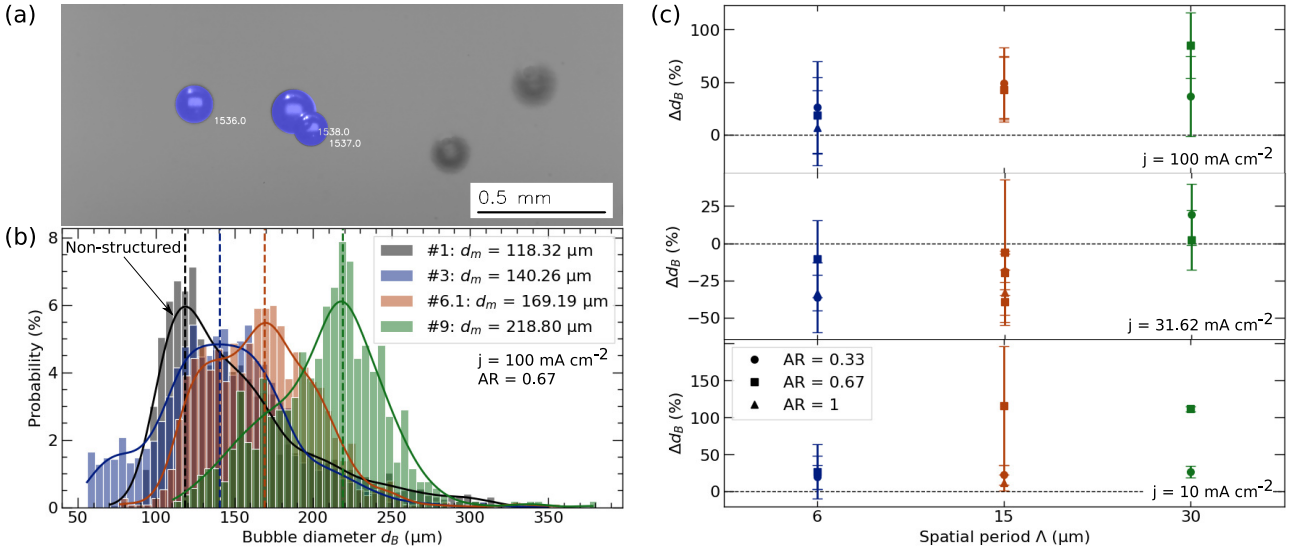


Figure 7: (a) Example sideview image with rising O_2 -bubbles. Those which are inside the focal plane are highlighted by blue color. The numbers represent the unique bubble IDs. (b) Detached bubble size distribution of all periods ($\Lambda(\#3) = 6 \mu\text{m}$, $\Lambda(\#6.1) = 15 \mu\text{m}$ and $\Lambda(\#9) = 30 \mu\text{m}$) at a constant $AR = 0.67$ in comparison to NSE (#1) and with mode value d_m of each bubble size distribution indicated by dash-dotted line. (c) Normalized change of d_m (see Eq. 12) at $j = 10, 31.62$ and 100 mA cm^{-2} .

A normalized metric was again defined for the discussion of the detached bubble sizes using the mode value of the bubble size distribution d_m to

$$\Delta d_B(j) = \frac{d_m(j) - d_{m, \text{NSE}}(j)}{d_{m, \text{NSE}}(j)}. \quad (12)$$

Due to few active nucleation sites at $j = 10 \text{ mA cm}^{-2}$, high spatial-resolution of the camera ($867.38 \text{ px mm}^{-1}$) and therefore few to no detected bubbles in the FOV, the evaluation was focused on higher j . In addition, as at $j = 100 \text{ mA cm}^{-2}$ the lowest η_{SS} was calculated (see Fig. 6 (b)), higher j were more relevant for the discussion of the improved electrode performance.

In Fig. 7 (c), it can be seen that at $j = 100 \text{ mA cm}^{-2}$ d_m was larger for all DLIP-structures compared to NSE. Moreover, increasing Λ led to increased d_m , with a maximum increase of $\Delta d_B \approx 80\%$ at $\Lambda = 30 \mu\text{m}$. However, the influence of AR on d_B had no clear tendency. At $j = 100 \text{ mA cm}^{-2}$, a clear influence of AR can only be observed for $\Lambda = 30 \mu\text{m}$, assuming larger d_B with increasing AR . However, the exact opposite is seen with a decreased current

density of $j = 31.62 \text{ mA cm}^{-2}$. The ambiguity is similarly evident in the obtained models for d_m ($R^2 = 0.812$) in Eq. 13 and d_{50} ($R^2 = 0.777$) in Eq. 14:

$$d_m = 113.17 + 18.745\bar{\Lambda} - 2.3123\bar{A}R + 35.806\bar{j} - 17.603\bar{A}R^2 + 28.066\bar{j}^2 \quad (13)$$

$$d_{50} = 106.18 + 18.361\bar{\Lambda} + 39.635\bar{j} + 27.49\bar{j}^2 \quad (14)$$

Interestingly, a significant influence of AR could be determined for d_m . Here, AR showed a negative influence on d_m , whereas AR was eliminated for d_{50} . Nevertheless, the factor of Λ was again found to be significant and greater for both models. It follows that Λ remains the most important parameter of the DLIP-structuring in terms of electrode performance and detached bubble size. Since $\dot{N}_{\text{O}_2} = \text{const.}$ is still valid for an applied j , it could be concluded that the number of bubbles and thus also the number of nucleation centers n_{nucl} was lower.

Active nucleation centers

This was confirmed by analysis of the recorded topview images. Therefore, bubbles sitting on the electrode were segmented using a trained stardist model and taken as a measure for active nucleation centers, as shown in Fig. 8 (a). Due to rising bubbles, the optical access to the electrode surface was limited after a specific time depending on the applied j . As shown in Fig. 8 (b) there was a maximum at $t = 1 \text{ min}$ for n_{nucl} at $j = 100 \text{ mA cm}^{-2}$. Therefore, depending on j only images within the first 4s, and 1s, were taken into account to calculate the time-averaged mean \bar{n}_{nucl} of the number of nucleation sites n_{nucl} at $j = 31.62 \text{ mA cm}^{-2}$ and $j = 100 \text{ mA cm}^{-2}$, respectively. Since few active nucleation sites and small \dot{N}_{O_2} , all recorded images were used for $j = 10 \text{ mA cm}^{-2}$. The normalized change in the number of active nucleation sites Δn_{nucl} was then calculated using the following equation:

$$\Delta n_{\text{nucl}}(j) = \frac{\bar{n}_{\text{nucl}}(j) - \bar{n}_{\text{nucl, NSE}}(j)}{\bar{n}_{\text{nucl, NSE}}(j)} \quad (15)$$

With the exception of DLIP-structures with $\Lambda = 6 \mu\text{m}$, all samples showed a clear decrease in Δn_{nucl} for all applied j , as shown in Fig. 8 (c). In addition, an increase in Λ led to a decrease in Δn_{nucl} . This could be attributed to the decrease in the number of peaks of the DLIP-structure with increasing Λ , as shown in the height profiles in Fig. 3 (b), where the bubbles are likely to grow.

In combination with the developed model for \bar{n}_{nucl} in Eq. 16 and the results of the bubble size analysis, it could be proven that the DLIP-structures strongly influence the bubble dynamic. Hereby, especially Λ showed a promising approach to tune d_B and decrease E_{cell} , as Λ was relevant for all developed models.

$$\ln(\bar{n}_{\text{nucl}}) = 1.5035 - 0.74842\bar{\Lambda} - 0.10964\bar{A}R + 1.4573\bar{j} - 0.33154\bar{\Lambda}\bar{A}R + 0.36201\bar{j}^2 \quad (16)$$

The shown improvement of the electrode performance in Fig. 6 (b) could also be explained by the bubble dynamics. As larger bubbles grew in fewer places on the electrode surface, it was ensured that the surface was largely wetted throughout. Thus, O_2 could be produced permanently. The dissolved gas was now seemingly collected by the bigger bubbles. From this it could be concluded that there were many active catalytic sites but only a low number of nucleation sites. This results in decreased η_Ω and following lower E were measured.

However, n_{nucl} could only be measured during few seconds, whereas d_B was measured during the full galvanostatic measurements of $t = 60 \text{ s}$. In addition, as only $\approx 35 \%$ of the entire electrode length of 10 mm was in the FOV in the topview and only $\approx 22 \%$ in the sideview, not all bubbles could be recorded. Especially at low j , this could lead to a systematic error if the

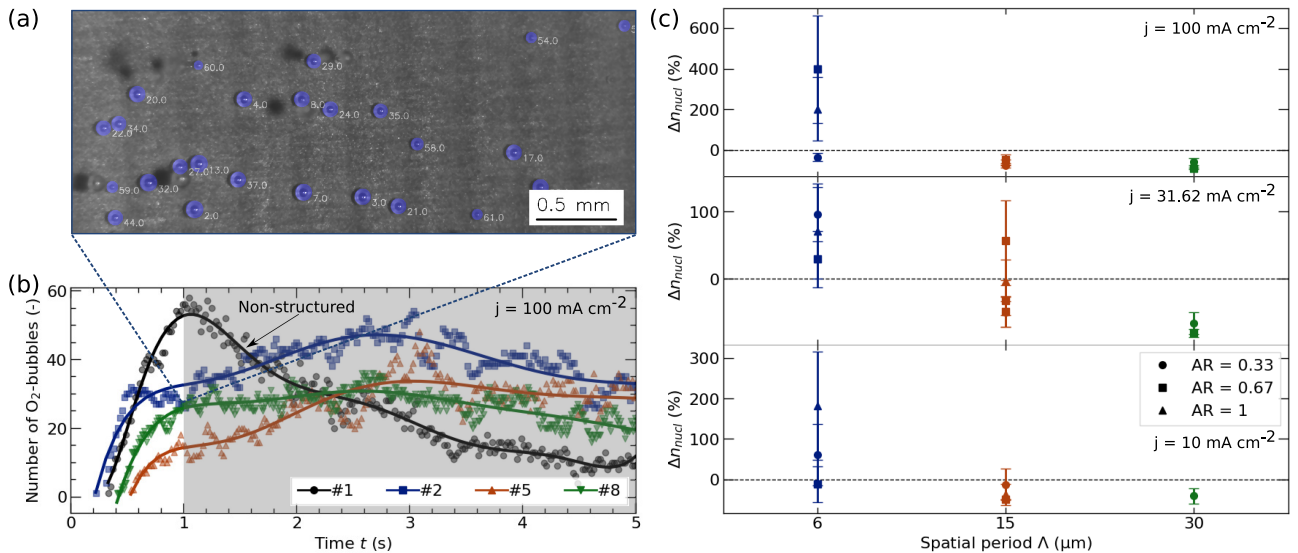


Figure 8: (a) Example topview image with highlighted O₂-bubbles growing on electrode #2 at $j = 100 \text{ mA cm}^{-2}$ and $t = 1 \text{ s}$. The numbers represent the unique bubble IDs. (b) Number of O₂-bubbles during 5 s galvanostatic measurements as a measure of n_{nuc} on all periods ($\Lambda(\#2) = 6 \mu\text{m}$, $\Lambda(\#5) = 15 \mu\text{m}$ and $\Lambda(\#8) = 30 \mu\text{m}$) at a constant $AR = 0.33$ in comparison to NSE (#1). Only data outside the gray shaded area is included in the further evaluation as rising bubbles are blocking the optical access. (c) Normalized n_{nuc} at $j = 10, 31.62$ and 100 mA cm^{-2} .

only active nucleation centers were located outside the FOV. Nevertheless, the measurement noise at the central point of DoE showed only a slight variation ($\sigma = 3.5447$)[†] for n_{nuc} . This further indicates that DLIP results in the formation of a homogeneous structure across the entire electrode. Furthermore, the application of a logarithmic transformation to the response prior to fitting resulted in very good results with $R^2 = 0.939$. It should be noted that for the model of \bar{n}_{nuc} , measurements 21 and 26 were excluded from the regression analysis due to the absence of nucleation sites within FOV.

Due to limited spatial resolution of the taken topview images, the exact nucleation sites could not be determined. However, as already mentioned above, all laser-structured electrodes showed superhydrophilic wetting behaviour. Exemplary images are shown in Fig. 9 (a) and Fig. S7 indicating the directional spreading of the DI-water along the DLIP line structures.[†] In addition, as all samples were cleaned in an ultrasonic bath and stored for at least 48 h in DI water, it can be assumed that only a negligible amount of gas pockets are present on the electrode surface, where bubbles are most likely to nucleate. It follows that a completely wetted surface is present at the beginning of each measurement. Due to the capillary forces acting in the channels, it can be further assumed that the electrode surface stays in a fully wetted state throughout the measurement. This leads to the assumption that bubbles are most likely to be pinned on the tips of the laser-structure as sketched in Fig. 9 (b). With increasing Λ the capillary forces decrease and thus, it can be assumed that the evolving bubbles covers the whole surface structure (see Fig. 9 (c)). However, these are hypothetical considerations that cannot be substantiated at this time.

Linear patterned nucleation sites

A special phenomena could be observed for the electrodes #3 and #4 with $\Lambda = 6 \mu\text{m}$ and $AR = 0.67$ and 1, respectively. During OER, the nucleation sites followed a linear pattern, as it is shown in Fig. 10 (a). The period of the visible dark/bright pattern of the electrode surface[†] as well as the distance between the observed lines of active nucleation sites was determined to

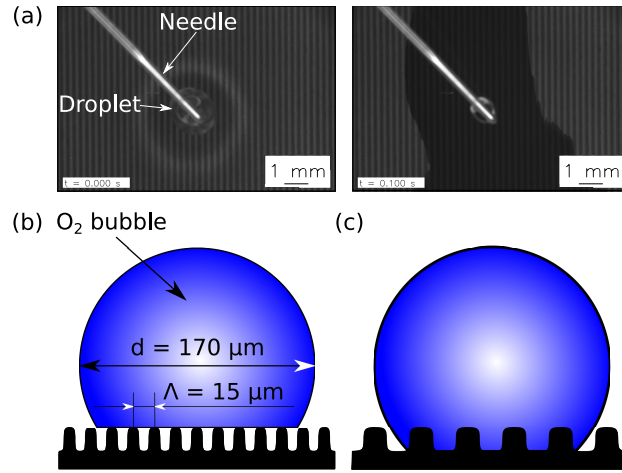


Figure 9: (a) Wetting behaviour of laser-structured surface showing superhydrophilic wetting as applied droplet spreads across entire surface. Full time series can be found in Fig. S7[†] (b) Possible nucleation of O_2 bubble with fully wetted with an assumed bubble size of $d_m = 170 \mu\text{m}$ according to Fig. 7 resulting in total of ≈ 11 covered periods for $\Lambda = 15 \mu\text{m}$. (c) Non-wetted electrode surface with increased Λ . Qualitative sketches throughout.

be equal to HD from the DLIP-process. As each laser pulse overlaps in x -distance with the previous pulse by HD , a superimposed intensity profile with a peak-to-peak distance equal to HD is found (see Fig. 10 (b)). This results in a darker surface in the region of the high intensity area (HIA) and a brighter surface in low intensity areas (LIA).

Initial assumptions of a changed oxide layer at the electrode surface could be invalidated with the help of XPS measurements, as there was no significant difference in the surface composition

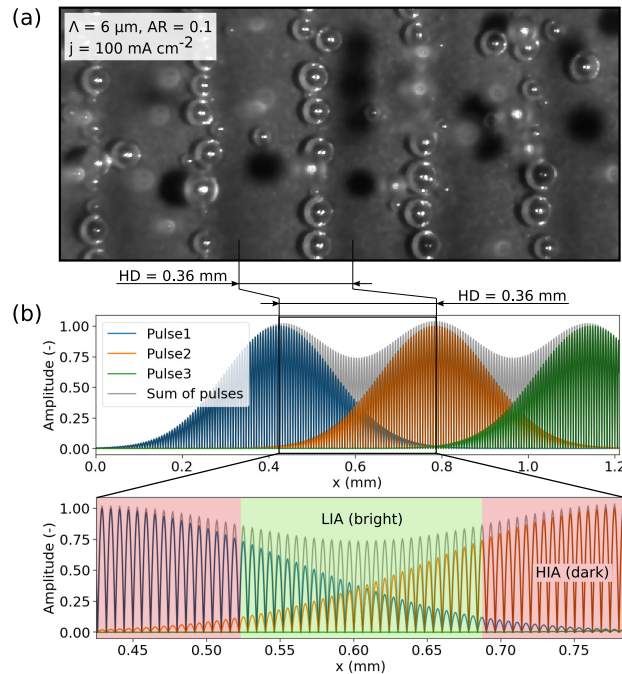


Figure 10: (a) Linear patterned O_2 bubble nucleation. (b) Superposition of several Gaussian interference patterns similar to the DLIP texturing for the period of $6 \mu\text{m}$ and the sum of all pulses showing a superimposed change in intensity with a period length equal to the hatch-distance. In addition, the high intensity area (HIA) and low intensity area (LIA) are highlighted in red and green, respectively.

between dark and bright areas. This is shown in Tab. 4, where the chemical states and surface concentrations of O and Ni were deconvoluted by fitting the XPS spectra (see Fig. S10 (c)). Therefore, the average value of the three measurements performed was calculated for both, HIA and LIA.

Table 4: Averaged surface composition and standard deviation (in atomic %) of the samples #3 and #4 determined by fitting XPS spectra in the high- (bright) and low intensity areas (dark)

Element	O			Ni	
BE (eV)	529.5	531.2	532.6	852.3	853.8
Groups/ Ox. state	O-Ni	O-Ni, O=C, O-Si	O-C, -OH, H ₂ O abs.	Ni ⁰	Ni ²⁺
#3 LIA	10.3 ± 0.5	12.7 ± 0.6	12.6 ± 0.9	1.0 ± 0.1	8.6 ± 0.4
#3 HIA	9.8 ± 1.1	13.2 ± 0.2	12.3 ± 0.6	1.1 ± 0.1	8.6 ± 0.6
#4 LIA	4.8 ± 0.3	22.5 ± 0.1	9.1 ± 0.1	0.5 ± 0.0	5.6 ± 0.0
#4 HIA	5.7 ± 0.5	21.1 ± 0.3	9.6 ± 0.1	0.3 ± 0.1	6.2 ± 0.4

Hence, the only significant difference between these areas must lie in the micro- and nanostructure of the electrode surface. This was shown using digital microscopy and SEM images. In lower intensity area (bright) a more shallow profile was detected compared to the higher intensity area (dark). In addition, SEM imaging showed microholes within the maxima region of the interference pattern, which are only present in the higher intensity area (see Fig. 4 and Fig. S6).[†] These could serve as cavities for the initial bubble nucleation.

This effect could be interesting with regard to optimized electrode surfaces and morphologies by defining nucleation sites through DLIP-structuring and optimizing the electrolyte flow at these sites. However, more studies are necessary to understand the ongoing mechanisms and long-term measurement have to be performed to proof that this phenomena does not change over time.

4 Conclusions

In summary, the influence of the structure parameters of DLIP, spatial period and aspect ratio, on the double-layer capacitance as a measure of the electrochemically active surface area was investigated. Additionally, the onset potential and overpotential during OER were analyzed. The relation between overpotential and bubble dynamics could be studied by determining the bubble size distribution and number of nucleation sites during galvanostatic measurements. For that purpose, Ni-foils were structured with line-like surface features with $\Lambda = 6, 15, 30 \mu\text{m}$ and $AR = 0.33, 0.67, 1.00$ using a ps pulsed laser and DLIP. By implementing a statistical design of experiments approach, models were derived from the measurements performed to analyze the significance of the influence of the structure parameters of laser-structuring.

An optimum of the spatial period was found for the double-layer capacitance, and thus the electrochemically active surface area, at $\Lambda = 15 \mu\text{m}$, which led to an increase by a factor of 12. In general, all laser-structured electrodes showed a significant enlargement of the electrochemically active surface area. Furthermore, the onset potential of OER could be decreased by $\approx 4.5\%$. However, at higher aspect ratios the homogeneity of the line-patterns was decreasing due to increased ablation and thus, a non-linear trend was observed.

The quasi-steady state potential, as a measure of the electrode overpotential, was decreased by up to $\approx 164 \text{mV}$ at $j = 100 \text{mA cm}^{-2}$. This shows the great potential of DLIP-structures for OER. As the bubble sizes were increased and the number of active nucleation sites was

decreased, the ohmic resistances could be decreased as large surface areas were wetted throughout. Furthermore, since no significant changes in the surface composition were found for the DLIP-structures, it could be inferred that the increased electrochemically active surface area provided more active catalytic sites. However, the dissolved gas was then collected by bigger bubbles at fewer nucleation sites on the DLIP-structured electrodes.

In general, the spatial period had a big impact on the overpotential and bubble dynamics, while the aspect ratio, and thus the depth of the structure, was not relevant for most models developed multiple regression analysis. Therefore, further studies should focus on the structure size instead of the depth.

It was found that the location of bubble nucleation could be tuned by the evolving laser-induced periodic surface structures. In conclusion, DLIP-structuring offers the possibility to enhance the overall efficiency of OER and thus, an AWE cell. Furthermore, DLIP-structuring might tune the detached bubble sizes to the needs of the periphery. Combined with the eventual possible definition of nucleation centers, this could facilitate the development of novel electrodes and even cell types.

Author Contributions

H.R.: Conceptualization, Investigation, Data curation, Formal Analysis, Methodology, Visualization, Writing - original draft, Editing; F.R.: Conceptualization, Investigation, Data curation, Formal Analysis, Methodology, Visualization, Writing - original draft, Editing; J.M.: Conceptualization, Formal Analysis, Methodology, Visualization, Writing - original draft, Editing; M.M.M.: Investigation, Formal Analysis, Writing - review & editing; K.S.: Investigation, Formal Analysis; R.B.: Investigation, Formal Analysis; H.H.: Conceptualization; X.Y.: Conceptualization, Supervision, Writing - review & editing; L.U.: Supervision, Writing - review & editing; A.F.L.: Conceptualization, Supervision, Writing - review & editing; K.E.: Funding acquisition, Project administration, Supervision, Writing - review & editing.

Conflicts of interest

There are no conflicts to declare.

Data availability

Data for this article, including electrochemical measurement data, raw images and relevant metadata of the performed experiments are available at RODARE at [10.14278/rodare.3064](https://doi.org/10.14278/rodare.3064).

Acknowledgments

This project is supported by the Federal State of Saxony in terms of the "European Regional Development Fund" (H2-EPF-HZDR), the Helmholtz Association Innovation pool project "Solar Hydrogen", the Hydrogen Lab of the School of Engineering of TU Dresden, and BMBF (project ALKALIMIT, grant no. 03SF0731A).

Bibliography

- [1] Mijndert van der Spek, Catherine Banet, Christian Bauer, Paolo Gabrielli, Ward Goldthorpe, Marco Mazzotti, Svend T. Munkejord, Nils A. Røkke, Nilay Shah, Nixon

- Sunny, Daniel Sutter, J. Martin Trusler, and Matteo Gazzani. Perspective on the hydrogen economy as a pathway to reach net-zero CO₂ emissions in Europe. *Energy Environ. Sci.*, 15(3):1034–1077, 2022. doi:[10.1039/d1ee02118d](https://doi.org/10.1039/d1ee02118d).
- [2] Iain Staffell, Daniel Scamman, Anthony Velazquez Abad, Paul Balcombe, Paul E. Dodds, Paul Ekins, Nilay Shah, and Kate R. Ward. The role of hydrogen and fuel cells in the global energy system. *Energy Environ. Sci.*, 12(2):463–491, 2019. doi:[10.1039/c8ee01157e](https://doi.org/10.1039/c8ee01157e).
- [3] Tom Smolinka and Jurgen Garche, editors. *Electrochemical Power Sources: Fundamentals, Systems, and Applications*. Elsevier, 2021. ISBN 9780128194249.
- [4] M. Hermesmann, K. Grübel, L. Scherotzki, and T. E. Müller. Promising pathways: The geographic and energetic potential of power-to-x technologies based on regeneratively obtained hydrogen. *Renew. Sust. Energ. Rev.*, 138:110644, 2021. doi:[10.1016/j.rser.2020.110644](https://doi.org/10.1016/j.rser.2020.110644).
- [5] Antonio Valente, Victor Tulus, Ángel Galán-Martín, Mark A. J. Huijbregts, and Gonzalo Guillén-Gosálbez. The role of hydrogen in heavy transport to operate within planetary boundaries. *Sustain. Energy Fuels*, pages 4637–4649, 2021. doi:[10.1039/d1se00790d](https://doi.org/10.1039/d1se00790d).
- [6] Laurens Van Hoecke, Ludovic Laffineur, Roy Campe, Patrice Perreault, Sammy W. Verbruggen, and Silvia Lenaerts. Challenges in the use of hydrogen for maritime applications. *Energy Environ. Sci.*, pages 815–843, 2021. doi:[10.1039/d0ee01545h](https://doi.org/10.1039/d0ee01545h).
- [7] R.R. Wang, Y.Q. Zhao, A. Babich, D. Senk, and X.Y. Fan. Hydrogen direct reduction (h-dr) in steel industry—an overview of challenges and opportunities. *J. Clean. Prod.*, 329:129797, 2021. ISSN 0959-6526. doi:[10.1016/j.jclepro.2021.129797](https://doi.org/10.1016/j.jclepro.2021.129797).
- [8] Dylan D. Furszyfer Del Rio, Benjamin K. Sovacool, Aoife M. Foley, Steve Griffiths, Morgan Bazilian, Jinsoo Kim, and David Rooney. Decarbonizing the glass industry: A critical and systematic review of developments, sociotechnical systems and policy options. *Renew. Sust. Energ. Rev.*, 155:111885, 2022. ISSN 1364-0321. doi:[10.1016/j.rser.2021.111885](https://doi.org/10.1016/j.rser.2021.111885).
- [9] Rami S. El-Emam and Hasan Özcan. Comprehensive review on the techno-economics of sustainable large-scale clean hydrogen production. *J. Clean. Prod.*, 220:593–609, 2019. ISSN 0959-6526. doi:[10.1016/j.jclepro.2019.01.309](https://doi.org/10.1016/j.jclepro.2019.01.309).
- [10] Yi He, Yifan Cui, Zhongxi Zhao, Yongtang Chen, Wenxu Shang, and Peng Tan. Strategies for bubble removal in electrochemical systems. *Energy Rev.*, 2(1):100015, mar 2023. doi:[10.1016/j.enrev.2023.100015](https://doi.org/10.1016/j.enrev.2023.100015).
- [11] Gerhard F. Swiegers, Richard N. L. Terrett, George Tsekouras, Takuya Tsuzuki, Ronald J. Pace, and Robert Stranger. The prospects of developing a highly energy-efficient water electrolyser by eliminating or mitigating bubble effects. *Sustain. Energy Fuels*, 5(5):1280–1310, 2021. doi:[10.1039/d0se01886d](https://doi.org/10.1039/d0se01886d).
- [12] Andrea Angulo, Peter van der Linde, Han Gardeniers, Miguel Modestino, and David Fernández Rivas. Influence of bubbles on the energy conversion efficiency of electrochemical reactors. *Joule*, 4(3):555–579, mar 2020. doi:[10.1016/j.joule.2020.01.005](https://doi.org/10.1016/j.joule.2020.01.005).
- [13] Kai Zeng and Dongke Zhang. Recent progress in alkaline water electrolysis for hydrogen production and applications. *Prog. Energy Combust. Sci.*, 36(3):307–326, 2010. doi:[10.1016/j.pecs.2009.11.002](https://doi.org/10.1016/j.pecs.2009.11.002).

- [14] H. Vogt. The quantities affecting the bubble coverage of gas-evolving electrodes. *Electrochim. Acta*, 235:495–499, may 2017. doi:[10.1016/j.electacta.2017.03.116](https://doi.org/10.1016/j.electacta.2017.03.116).
- [15] Helmut Vogt and Karl Stephan. Local microprocesses at gas-evolving electrodes and their influence on mass transfer. *Electrochim. Acta*, 155:348–356, feb 2015. doi:[10.1016/j.electacta.2015.01.008](https://doi.org/10.1016/j.electacta.2015.01.008).
- [16] H. Vogt. On the gas-evolution efficiency of electrodes I - Theoretical. *Electrochim. Acta*, 56(3):1409–1416, 2011. doi:[10.1016/j.electacta.2010.08.101](https://doi.org/10.1016/j.electacta.2010.08.101).
- [17] R. J. Balzer and H. Vogt. Effect of electrolyte flow on the bubble coverage of vertical gas-evolving electrodes. *J. Electrochem. Soc.*, 150(1):E11, 2003. ISSN 0013-4651. doi:[10.1149/1.1524185](https://doi.org/10.1149/1.1524185).
- [18] J. Eigeldinger and H. Vogt. The bubble coverage of gas-evolving electrodes in a flowing electrolyte. *Electrochim. Acta*, 45(27):4449–4456, 2000. ISSN 0013-4686. doi:[10.1016/S0013-4686\(00\)00513-2](https://doi.org/10.1016/S0013-4686(00)00513-2).
- [19] Fernando Rocha, Renaud Delmelle, Christos Georgiadis, and Joris Proost. Effect of pore size and electrolyte flow rate on the bubble removal efficiency of 3d pure ni foam electrodes during alkaline water electrolysis. *J. Environ. Chem. Eng.*, 10(3):107648, June 2022. ISSN 2213-3437. doi:[10.1016/j.jece.2022.107648](https://doi.org/10.1016/j.jece.2022.107648).
- [20] Yan-Hom Li and Yen-Ju Chen. The effect of magnetic field on the dynamics of gas bubbles in water electrolysis. *Sci. Rep.*, 11(1):9346, April 2021. ISSN 2045-2322. doi:[10.1038/s41598-021-87947-9](https://doi.org/10.1038/s41598-021-87947-9).
- [21] Ghasem Barati Darband, Mahmood Aliofkhazraei, and Sangaraju Shanmugam. Recent advances in methods and technologies for enhancing bubble detachment during electrochemical water splitting. *Renew. Sust. Energ. Rev.*, 114:109300, oct 2019. doi:[10.1016/j.rser.2019.109300](https://doi.org/10.1016/j.rser.2019.109300).
- [22] Dominik Baczyzmalski, Franziska Karnbach, Gerd Mutschke, Xuegeng Yang, Kerstin Eckert, Margitta Uhlemann, and Christian Cierpka. Growth and detachment of single hydrogen bubbles in a magnetohydrodynamic shear flow. *Phys. Rev. Fluids*, 2(9):093701, September 2017. ISSN 2469-990X. doi:[10.1103/physrevfluids.2.093701](https://doi.org/10.1103/physrevfluids.2.093701).
- [23] Jakub Adam Koza, Sascha Mühlhoff, Piotr Żabiński, Petr A. Nikrityuk, Kerstin Eckert, Margitta Uhlemann, Annett Gebert, Tom Weier, Ludwig Schultz, and Stefan Odenbach. Hydrogen evolution under the influence of a magnetic field. *Electrochimica Acta*, 56(6):2665–2675, February 2011. ISSN 0013-4686. doi:[10.1016/j.electacta.2010.12.031](https://doi.org/10.1016/j.electacta.2010.12.031).
- [24] Takami Iida, Hisayoshi Matsushima, and Y. Fukunaka. Water Electrolysis under a Magnetic Field. *J. Electrochem. Soc.*, 154:E112–E115, 2007. doi:[10.1149/1.2742807](https://doi.org/10.1149/1.2742807).
- [25] Aleksandr Bashkatov, Sunghak Park, Çayan Demirkır, Jeffery A. Wood, Marc T. M. Koper, Detlef Lohse, and Dominik Krug. Performance enhancement of electrocatalytic hydrogen evolution through coalescence-induced bubble dynamics. *J. Am. Chem. Soc.*, 146(14):10177–10186, 2024. doi:[10.1021/jacs.4c02018](https://doi.org/10.1021/jacs.4c02018).
- [26] Pengyu Lv, Pablo Peñas, Hai Le The, Jan Eijkel, Albert van den Berg, Xuehua Zhang, and Detlef Lohse. Self-propelled detachment upon coalescence of surface bubbles. *Phys. Rev. Lett.*, 127(23):235501, nov 2021. doi:[10.1103/physrevlett.127.235501](https://doi.org/10.1103/physrevlett.127.235501).

- [27] Shilong Jiao, Xianwei Fu, Shuangyin Wang, and Yong Zhao. Perfecting electrocatalysts via imperfections: towards the large-scale deployment of water electrolysis technology. *Energy Environ. Sci.*, 14(4):1722–1770, 2021. doi:[10.1039/d0ee03635h](https://doi.org/10.1039/d0ee03635h).
- [28] Yang Yang, Jun Li, Yingrui Yang, Linghan Lan, Run Liu, Qian Fu, Liang Zhang, Qiang Liao, and Xun Zhu. Gradient porous electrode-inducing bubble splitting for highly efficient hydrogen evolution. *Appl. Energy*, 307:118278, feb 2022. doi:[10.1016/j.apenergy.2021.118278](https://doi.org/10.1016/j.apenergy.2021.118278).
- [29] Tianyi Kou, Shanwen Wang, Rongpei Shi, Tao Zhang, Samuel Chiovoloni, Jennifer Q. Lu, Wen Chen, Marcus A. Worsley, Brandon C. Wood, Sarah E. Baker, Eric B. Duoss, Rui Wu, Cheng Zhu, and Yat Li. Periodic porous 3d electrodes mitigate gas bubble traffic during alkaline water electrolysis at high current densities. *Adv. Energy Mater.*, 10(46):2002955, oct 2020. doi:[10.1002/aenm.202002955](https://doi.org/10.1002/aenm.202002955).
- [30] Tatsuki Fujimura, Masahiro Kunimoto, Yasuhiro Fukunaka, and Takayuki Homma. Analysis of the hydrogen evolution reaction at ni micro-patterned electrodes. *Electrochim. Acta*, 368:137678, February 2021. ISSN 0013-4686. doi:[10.1016/j.electacta.2020.137678](https://doi.org/10.1016/j.electacta.2020.137678).
- [31] R. Andaveh, Gh. Barati Darband, M. Maleki, and A. Sabour Rouhaghdam. Superaerophobic/superhydrophilic surfaces as advanced electrocatalysts for the hydrogen evolution reaction: a comprehensive review. *J. Mater. Chem. A*, 10(10):5147–5173, 2022. ISSN 2050-7496. doi:[10.1039/d1ta10519a](https://doi.org/10.1039/d1ta10519a).
- [32] Dongke Zhang and Kai Zeng. Evaluating the behavior of electrolytic gas bubbles and their effect on the cell voltage in alkaline water electrolysis. *Ind. Eng. Chem. Res.*, 51(42):13825–13832, 2012. doi:[10.1021/ie301029e](https://doi.org/10.1021/ie301029e).
- [33] Aleksandr Bashkatov, Syed Sahil Hossain, Gerd Mutschke, Xuegeng Yang, Hannes Rox, Inez M. Weidinger, and Kerstin Eckert. On the growth regimes of hydrogen bubbles at microelectrodes. *Phys. Chem. Chem. Phys.*, 24(43):26738–26752, 2022. ISSN 1463-9084. doi:[10.1039/d2cp02092k](https://doi.org/10.1039/d2cp02092k).
- [34] Julian Massing, Gerd Mutschke, Dominik Baczyzmalski, Syed Sahil Hossain, Xuegeng Yang, Kerstin Eckert, and Christian Cierpka. Thermocapillary convection during hydrogen evolution at microelectrodes. *Electrochim. Acta*, 297:929–940, 2019. doi:[10.1016/j.electacta.2018.11.187](https://doi.org/10.1016/j.electacta.2018.11.187).
- [35] Xuegeng Yang, Dominik Baczyzmalski, Christian Cierpka, Gerd Mutschke, and Kerstin Eckert. Marangoni convection at electrogenerated hydrogen bubbles. *Phys. Chem. Chem. Phys.*, 20(17):11542–11548, 2018. doi:[10.1039/c8cp01050a](https://doi.org/10.1039/c8cp01050a).
- [36] A.M. Meulenbroek, A.W. Vreman, and N.G. Deen. Competing marangoni effects form a stagnant cap on the interface of a hydrogen bubble attached to a microelectrode. *Electrochim. Acta*, page 138298, 2021. doi:[10.1016/j.electacta.2021.138298](https://doi.org/10.1016/j.electacta.2021.138298).
- [37] Géraldine Duhar and Catherine Colin. Dynamics of bubble growth and detachment in a viscous shear flow. *Phys. Fluids*, 18(7):077101, jul 2006. ISSN 1089-7666. doi:[10.1063/1.2213638](https://doi.org/10.1063/1.2213638).
- [38] J.W. Haverkort. A general mass transfer equation for gas-evolving electrodes. *Int. J. Hydrog. Energy*, 74:283–296, July 2024. ISSN 0360-3199. doi:[10.1016/j.ijhydene.2024.06.010](https://doi.org/10.1016/j.ijhydene.2024.06.010).

- [39] N. P. Brandon, G. H. Kelsall, S. Levine, and A. L. Smith. Interfacial electrical properties of electrogenerated bubbles. *J. Appl. Electrochem.*, 15(4):485–493, jul 1985. doi:[10.1007/bf01059289](https://doi.org/10.1007/bf01059289).
- [40] N. P. Brandon and G. H. Kelsall. Growth kinetics of bubbles electrogenerated at micro-electrodes. *J. Appl. Electrochem.*, 15:475–484, 1985. doi:[10.1007/BF01059288](https://doi.org/10.1007/BF01059288).
- [41] Run Shi, Lu Shang, and Tierui Zhang. Three phase interface engineering for advanced catalytic applications. *ACS Appl. Energy Mater.*, 4(2):1045–1052, January 2021. ISSN 2574-0962. doi:[10.1021/acsaem.0c02989](https://doi.org/10.1021/acsaem.0c02989).
- [42] Byung Keun Kim, Myung Jun Kim, and Jae Jeong Kim. Impact of surface hydrophilicity on electrochemical water splitting. *ACS Appl. Mater. Interfaces*, 13(10):11940–11947, March 2021. ISSN 1944-8252. doi:[10.1021/acsami.0c22409](https://doi.org/10.1021/acsami.0c22409).
- [43] L. Krause, K. Skibińska, H. Rox, R. Baumann, M. M. Marzec, X. Yang, G. Mutschke, P. Żabiński, A. F. Lasagni, and K. Eckert. Hydrogen bubble size distribution on nanostructured ni surfaces: Electrochemically active surface area versus wettability. *ACS Appl. Mater. Interfaces*, 15(14):18290–18299, apr 2023. doi:[10.1021/acsami.2c22231](https://doi.org/10.1021/acsami.2c22231).
- [44] Katarzyna Skibińska, Konrad Wojtaszek, Lukas Krause, Anna Kula, Xuegeng Yang, Mateusz M. Marzec, Marek Wojnicki, and Piotr Żabiński. Tuning up catalytical properties of electrochemically prepared nanoconical co-ni deposit for her and oer. *Appl. Surf. Sci.*, 607:155004, January 2023. ISSN 0169-4332. doi:[10.1016/j.apsusc.2022.155004](https://doi.org/10.1016/j.apsusc.2022.155004).
- [45] Qiu Ren, Longsheng Feng, Congwang Ye, Xinzhe Xue, Dun Lin, Samuel Eisenberg, Tianyi Kou, Eric B. Duoss, Cheng Zhu, and Yat Li. Nanocone-modified surface facilitates gas bubble detachment for high-rate alkaline water splitting. *Adv. Energy Mater.*, 13(39):2302073, sep 2023. doi:[10.1002/aenm.202302073](https://doi.org/10.1002/aenm.202302073).
- [46] Ömer Akay, Jeffrey Poon, Craig Robertson, Fatwa Firdaus Abdi, Beatriz Roldan Cuenya, Michael Giersig, and Katharina Brinkert. Releasing the bubbles: Nanotopographical electrocatalyst design for efficient photoelectrochemical hydrogen production in microgravity environment. *Adv. Sci.*, 9(8):2105380, 2022. doi:[10.1002/advs.202105380](https://doi.org/10.1002/advs.202105380).
- [47] Katharina Brinkert, Matthias H. Richter, Ömer Akay, Janine Liedtke, Michael Giersig, Katherine T. Fountaine, and Hans-Joachim Lewerenz. Efficient solar hydrogen generation in microgravity environment. *Nat. Commun.*, 9(1):2527, July 2018. ISSN 2041-1723. doi:[10.1038/s41467-018-04844-y](https://doi.org/10.1038/s41467-018-04844-y).
- [48] Fabian Ränke, Robert Baumann, Bogdan Voisiat, Marcos Soldera, and Andrés Fabián Lasagni. Nano/microstructuring of nickel electrodes by combining direct laser interference patterning and polygon scanner processing for efficient hydrogen production. *Adv. Eng. Mater.*, 26(10):2301583, 2024. doi:[10.1002/adem.202301583](https://doi.org/10.1002/adem.202301583).
- [49] Fabian Ränke, Robert Baumann, Bogdan Voisiat, and Andrés Fabián Lasagni. High throughput laser surface micro-structuring of polystyrene by combining direct laser interference patterning with polygon scanner technology. *Mater. Lett. X*, 14:100144, 2022. ISSN 2590-1508. doi:[10.1016/j.mlblux.2022.100144](https://doi.org/10.1016/j.mlblux.2022.100144).
- [50] Robert Baumann, Thomas Rauscher, Christian Immanuel Bernäcker, Christoph Zwahr, Thomas Weißgärber, Lars Röntzsch, and Andrés Fabián Lasagni. Laser structuring of open cell metal foams for micro scale surface enlargement. *J. Laser Micro/Nanoeng.*, pages 132–138, sep 2020. doi:[10.2961/jlmn.2020.02.2010](https://doi.org/10.2961/jlmn.2020.02.2010).

- [51] Matthias Koj, Thomas Gimpel, Wolfgang Schade, and Thomas Turek. Laser structured nickel-iron electrodes for oxygen evolution in alkaline water electrolysis. *Int. J. Hydrog. Energy*, 44(25):12671–12684, may 2019. doi:[10.1016/j.ijhydene.2019.01.030](https://doi.org/10.1016/j.ijhydene.2019.01.030).
- [52] Thomas Rauscher, Christian Immanuel Müller, Andreas Gabler, Thomas Gimpel, Michael Köhring, Bernd Kieback, Wolfgang Schade, and Lars Röntzsch. Femtosecond-laser structuring of ni electrodes for highly active hydrogen evolution. *Electrochim. Acta*, 247:1130–1139, sep 2017. doi:[10.1016/j.electacta.2017.07.074](https://doi.org/10.1016/j.electacta.2017.07.074).
- [53] Alex R. Neale, Yang Jin, Jinglei Ouyang, Stephen Hughes, David Hesp, Vinod Dhanak, Geoff Dearden, Stuart Edwardson, and Laurence J. Hardwick. Electrochemical performance of laser micro-structured nickel oxyhydroxide cathodes. *J. Power Sources*, 271:42–47, December 2014. ISSN 0378-7753. doi:[10.1016/j.jpowsour.2014.07.167](https://doi.org/10.1016/j.jpowsour.2014.07.167).
- [54] Andrés F. Lasagni, Carsten Gachot, Kim E. Trinh, Michael Hans, Andreas Rosenkranz, Teja Roch, Sebastian Eckhardt, Tim Kunze, Matthias Bieda, Denise Günther, Valentin Lang, and Frank Mücklich. Direct laser interference patterning, 20 years of development: from the basics to industrial applications. In Udo Klotzbach, Kunihiko Washio, and Rainer Kling, editors, *Laser-based Micro- and Nanoprocessing XI*. SPIE, February 2017. doi:[10.1117/12.2252595](https://doi.org/10.1117/12.2252595).
- [55] J. A. Wahab, M. J. Ghazali, W. M. W. Yusoff, and Z. Sajuri. Enhancing material performance through laser surface texturing: a review. *Trans. IMF*, 94(4):193–198, July 2016. ISSN 1745-9192. doi:[10.1080/00202967.2016.1191141](https://doi.org/10.1080/00202967.2016.1191141).
- [56] G. R. B. E. Römer, J. Z. P. Skolski, J. Vincenc Oboňa, V. Ocelík, J. T. M. de Hosson, and A. J. Huis in 't Veld. Laser-induced periodic surface structures, modeling, experiments, and applications. In Udo Klotzbach, Kunihiko Washio, and Craig B. Arnold, editors, *Laser-based Micro- and Nanoprocessing VIII*, volume 8968, page 89680D. International Society for Optics and Photonics, SPIE, 2014. doi:[10.1117/12.2037541](https://doi.org/10.1117/12.2037541).
- [57] J. E. Sipe, Jeff F. Young, J. S. Preston, and H. M. van Driel. Laser-induced periodic surface structure. i. theory. *Phys. Rev. B*, 27:1141–1154, 1983. doi:[10.1103/PhysRevB.27.1141](https://doi.org/10.1103/PhysRevB.27.1141).
- [58] Jörn Bonse, Sabrina V. Kirner, Sandra Höhm, Nadja Epperlein, Dirk Spaltmann, Arkadi Rosenfeld, and Jörg Krüger. Applications of laser-induced periodic surface structures (LIPSS). In Udo Klotzbach, Kunihiko Washio, and Rainer Kling, editors, *Laser-based Micro- and Nanoprocessing XI*, volume 10092, page 100920N. International Society for Optics and Photonics, SPIE, 2017. doi:[10.1117/12.2250919](https://doi.org/10.1117/12.2250919).
- [59] Viktor Hoffmann, Luise Hoffmann, Wolfgang Schade, Thomas Turek, and Thomas Gimpel. Femtosecond laser molybdenum alloyed and enlarged nickel surfaces for the hydrogen evolution reaction in alkaline water electrolysis. *International Journal of Hydrogen Energy*, 47(48):20729–20740, 2022. ISSN 0360-3199. doi:<https://doi.org/10.1016/j.ijhydene.2022.04.194>.
- [60] Zaiwei Cai, Zihao Li, Yingtao Zhang, Chiyi Wei, Hao Tian, Molei Hao, Xiaoming Wei, and Zhongmin Yang. High repetition rate ultrafast laser-structured nickel electrocatalyst for efficient hydrogen evolution reaction. *Advanced Photonics Nexus*, 2(5):056009, 2023. doi:[10.1117/1.APN.2.5.056009](https://doi.org/10.1117/1.APN.2.5.056009).
- [61] Fabian Ränke, Stephan Moghtaderifard, Lis Zschach, Robert Baumann, Bogdan Voisiat, Marcos Soldara, Leonard Günther, Sebastian Hilbert, Christian Immanuel Bernäcker, Thomas Weißgärber, and Andrés Fabián Lasagni. Femtosecond direct laser interference

- patterning of nickel electrodes for improving electrochemical properties. *J. Laser Micro Nanoeng.*, pages 102–110, September 2004. ISSN 1880-0688. doi:[10.2961/jlmn.2024.02.2002](https://doi.org/10.2961/jlmn.2024.02.2002).
- [62] Emiliana Fabbri and Thomas J. Schmidt. Oxygen evolution reaction—the enigma in water electrolysis. *ACS Catal.*, 8(10):9765–9774, September 2018. ISSN 2155-5435. doi:[10.1021/acscatal.8b02712](https://doi.org/10.1021/acscatal.8b02712).
- [63] Nian-Tzu Suen, Sung-Fu Hung, Quan Quan, Nan Zhang, Yi-Jun Xu, and Hao Ming Chen. Electrocatalysis for the oxygen evolution reaction: recent development and future perspectives. *Chem. Soc. Rev.*, 46(2):337–365, 2017. ISSN 1460-4744. doi:[10.1039/c6cs00328a](https://doi.org/10.1039/c6cs00328a).
- [64] Robert Lee. Statistical Design of Experiments for Screening and Optimization. *Chem. Ing. Tech.*, 91(3):191–200, 2019. ISSN 0009-286X, 1522-2640. doi:[10.1002/cite.201800100](https://doi.org/10.1002/cite.201800100).
- [65] Andrés Fabian Lasagni and Bogdan Voisiat. Anordnung optischer elemente zur ausbildung von großflächigen strukturen mit linienförmigen strukturelementen, 2021. No. DE102020204656A1.
- [66] H. Rox, A. Bashkatov, X. Yang, S. Loos, G. Mutschke, G. Gerbeth, and K. Eckert. Bubble size distribution and electrode coverage at porous nickel electrodes in a novel 3-electrode flow-through cell. *Int. J. Hydrog. Energy*, 48(8):2892–2905, 2023. doi:[10.1016/j.ijhydene.2022.10.165](https://doi.org/10.1016/j.ijhydene.2022.10.165).
- [67] Julian Heinrich, Fabian Ränke, Karin Schwarzenberger, Xuegeng Yang, Robert Baumann, Mateusz Marzec, Andrés Fabián Lasagni, and Kerstin Eckert. Functionalization of ti64 via direct laser interference patterning and its influence on wettability and oxygen bubble nucleation. *Langmuir*, 40(6):2918–2929, 2024. doi:[10.1021/acs.langmuir.3c02863](https://doi.org/10.1021/acs.langmuir.3c02863).
- [68] Uwe Schmidt, Martin Weigert, Coleman Broaddus, and Gene Myers. Cell detection with star-convex polygons. In *Medical Image Computing and Computer Assisted Intervention - MICCAI 2018 - 21st International Conference, Granada, Spain, September 16-20, 2018, Proceedings, Part II*, pages 265–273, 2018. doi:[10.1007/978-3-030-00934-2_30](https://doi.org/10.1007/978-3-030-00934-2_30).
- [69] Martin Weigert, Uwe Schmidt, Robert Haase, Ko Sugawara, and Gene Myers. Star-convex polyhedra for 3d object detection and segmentation in microscopy. In *The IEEE Winter Conference on Applications of Computer Vision (WACV)*, March 2020. doi:[10.1109/WACV45572.2020.9093435](https://doi.org/10.1109/WACV45572.2020.9093435).
- [70] Daniel B. Allan, Thomas Caswell, Nathan C. Keim, Casper M. van der Wel, and Ruben W. Verweij. `soft-matter/trackpy`: v0.6.1, February 2023.
- [71] HuaZhong Zhu, HongChao Zhang, XiaoWu Ni, ZhongHua Shen, and Jian Lu. Fabrication of superhydrophilic surface on metallic nickel by sub-nanosecond laser-induced ablation. *AIP Advances*, 9(8):085308, 2019. ISSN 2158-3226. doi:[10.1063/1.5111069](https://doi.org/10.1063/1.5111069).
- [72] Christian Schäfer, Pablo Maria Delfino, Philipp Leonhard-Trautmann, Vincent Ott, Sebastian Suarez, Michael Stüber, Frank Mücklich, and Christoph Pauly. Fabrication of smooth, periodic surface structures: Combining direct laser interference patterning and electropolishing. *Advanced Engineering Materials*, page 2400435, 2024. doi:[10.1002/adem.202400435](https://doi.org/10.1002/adem.202400435).
- [73] J. Bonse, J. Krüger, S. Höhm, and A. Rosenfeld. Femtosecond laser-induced periodic surface structures. *Journal of Laser Applications*, 24(4):042006, 2012. ISSN 1042-346X. doi:[10.2351/1.4712658](https://doi.org/10.2351/1.4712658).

- [74] Jörn Bonse and Stephan Gräf. Maxwell meets marangoni—a review of theories on laser-induced periodic surface structures. *Laser & Photonics Reviews*, 14(10):2000215, 2020. doi:[10.1002/lpor.202000215](https://doi.org/10.1002/lpor.202000215).
- [75] Alfredo I. Aguilar-Morales, Sabri Alamri, and Andrés Fabián Lasagni. Micro-fabrication of high aspect ratio periodic structures on stainless steel by picosecond direct laser interference patterning. *Journal of Materials Processing Technology*, 252:313–321, 2018. ISSN 0924-0136. doi:[10.1016/j.jmatprotec.2017.09.039](https://doi.org/10.1016/j.jmatprotec.2017.09.039).
- [76] Huagang Liu, Wenxiong Lin, Zhenyuan Lin, Lingfei Ji, and Minghui Hong. Self-organized periodic microholes array formation on aluminum surface via femtosecond laser ablation induced incubation effect. *Advanced Functional Materials*, 29(42):1903576, 2019. doi:[10.1002/adfm.201903576](https://doi.org/10.1002/adfm.201903576).
- [77] Christian I. Bernäcker, Thomas Gimpel, Alexander Bomm, Thomas Rauscher, Sebastian Mauermann, Mingji Li, Eike G. Hübner, Wolfgang Schade, and Lars Röntzsch. Short pulse laser structuring as a scalable process to produce cathodes for large alkaline water electrolyzers. *J. Power Sources*, 538:231572, 2022. doi:[10.1016/j.jpowsour.2022.231572](https://doi.org/10.1016/j.jpowsour.2022.231572).
- [78] Xueqi Pang, Jonathan T. Davis, Albert D. Harvey Ill, and Daniel V. Esposito. Framework for evaluating the performance limits of membraneless electrolyzers. *Energy Environ. Sci.*, 13:3663–3678, 2020. doi:[10.1039/d0ee02268c](https://doi.org/10.1039/d0ee02268c).
- [79] Vincent S. J. Craig, Barry W. Ninham, and Richard M. Pashley. The effect of electrolytes on bubble coalescence in water. *J. Phys. Chem.*, 97(39):10192–10197, sep 1993. doi:[10.1021/j100141a047](https://doi.org/10.1021/j100141a047).
- [80] G. Beamson and D. Briggs. High resolution xps of organic polymers. the scienta esca 300 database. *J. Chem. Educ.*, 70:A25, 1993. doi:[10.1021/ed070pA25.5](https://doi.org/10.1021/ed070pA25.5).
- [81] Paul G Rouxhet and Michel J Genet. Xps analysis of bio-organic systems. *Surf. Interface Anal.*, 43(12):1453–1470, 2011. doi:[10.1002/sia.3831](https://doi.org/10.1002/sia.3831).
- [82] Nan Liu, Tong Li, Ziqiong Zhao, Jing Liu, Xiaoguang Luo, Xiaohong Yuan, Kun Luo, Julong He, Dongli Yu, and Yuanchun Zhao. From triazine to heptazine: origin of graphitic carbon nitride as a photocatalyst. *ACS Omega*, 5(21):12557–12567, 2020. doi:[10.1021/acsomega.0c01607](https://doi.org/10.1021/acsomega.0c01607).
- [83] Michel J. Genet, Christine C. Dupont-Gillain, and Paul G. Rouxhet. Xps analysis of biosystems and biomaterials. In Egon Matijevic, editor, *Medical applications of colloids*, volume 177, pages 177–307. Springer, 2008. doi:[10.1007/978-0-387-76921-9](https://doi.org/10.1007/978-0-387-76921-9).
- [84] C. D. Wagner, D. E. Passoja, H. F. Hillery, T. G. Kinisky, H. A. Six, W. T. Jansen, and J. A. Taylor. Auger and photoelectron line energy relationships in aluminum–oxygen and silicon–oxygen compounds. *J. Vac. Sci. Technol.*, 21(4):933–944, 1982. doi:[10.1116/1.571870](https://doi.org/10.1116/1.571870).
- [85] A.D. Wagner, A.V. Naumkin, A. Kraut-Vass, J.W. Allison, C.J. Powell, and J.R.J. Rumble, 2003. URL <http://srdata.nist.gov/xps/>.
- [86] Marzia Fantauzzi, Bernhard Elsener, Davide Atzei, Americo Rigoldi, and Antonella Rossi. Exploiting xps for the identification of sulfides and polysulfides. *RSC Adv.*, 5(93):75953–75963, 2015. doi:[10.1039/C5RA14915K](https://doi.org/10.1039/C5RA14915K).

- [87] Mark C. Biesinger, Brad P. Payne, Leo W. M. Lau, Andrea Gerson, and Roger St. C. Smart. X-ray photoelectron spectroscopic chemical state quantification of mixed nickel metal, oxide and hydroxide systems. *Surf. Interface Anal.*, 41(4):324–332, 2009. doi:[10.1002/sia.3026](https://doi.org/10.1002/sia.3026).
- [88] Mark C. Biesinger, Brad P. Payne, Andrew P. Grosvenor, Leo W. M. Lau, Andrea R. Gerson, and Roger St. C. Smart. Resolving surface chemical states in xps analysis of first row transition metals, oxides and hydroxides: Cr, mn, fe, co and ni. *Appl. Surf. Sci.*, 257(7):2717–2730, 2011. doi:[10.1016/j.apsusc.2010.10.051](https://doi.org/10.1016/j.apsusc.2010.10.051).
- [89] Mark C. Biesinger, Leo W. M. Lau, Andrea R. Gerson, and Roger St. C. Smart. The role of the auger parameter in xps studies of nickel metal, halides and oxides. *Phys. Chem. Chem. Phys.*, 14(7):2434–2442, 2012. doi:[10.1039/C2CP22419D](https://doi.org/10.1039/C2CP22419D).

Electronic supplementary information: Boosting electrode performance and bubble management via Direct Laser Interference Patterning

S1 Design of Experiments

Full-factorial design

Table S1: Randomized experiment sequence according to full-factorial design for galvanostatic measurements with dropped experiments for $\Lambda = 30\ \mu\text{m}$ and $AR = 1.0$ as this structure could not be manufactured reproducibly

Exp. No.	Λ (μm)	AR (-)	j (mA cm^{-2})
1	6.00	0.33	10.00
2	30.00	0.33	100.00
3	30.00	0.33	31.62
4	6.00	1.00	10.00
5	6.00	1.00	100.00
6	15.00	1.00	31.62
7	15.00	0.67	31.62
8	6.00	0.33	31.62
9	15.00	0.67	100.00
10	30.00	0.67	31.62
11	6.00	0.67	10.00
12	15.00	1.00	10.00
13	15.00	0.33	10.00
14	30.00	0.67	100.00
15	6.00	0.33	100.00
16	15.00	0.33	100.00
17	6.00	1.00	31.62
18	15.00	0.33	31.62
19	15.00	0.67	31.62
20	6.00	0.67	31.62
21	15.00	0.67	10.00
22	6.00	0.67	100.00
23	30.00	0.33	10.00
24	15.00	1.00	100.00
25	15.00	0.67	31.62
26	30.00	0.67	10.00
27		NSE	10.00
28		NSE	31.62
29		NSE	100.00

S2 Preliminary experiments on DLIP

In the first set of experiments, nickel substrates were irradiated using the two-beam DLIP configuration to generate line shaped surface features, exhibiting spatial periods of 6.0, 15.0 and 30.0 μm . As process parameter the number of consecutive passes N were varied from 1 to 45 to evaluate their influence on the resulting structure morphology and aspect ratio AR . For

this purpose, the total amount of energy that is used to irradiate a certain area (cumulated laser fluence Φ_{cum}) has been calculated using Eq. S1 and S2:

$$N_{\text{pulses}} = \frac{d_y \cdot f_{\text{rep}}}{v_{\text{scan}}} \quad (\text{S1})$$

$$\Phi_{\text{cum}} = \frac{E_p}{A_{\text{spot}}} \cdot N_{\text{pulses}} \cdot N, \quad (\text{S2})$$

where N_{pulses} denotes the number of laser pulses irradiating the same effective area. In this context, the pulse-to-pulse distance of $5 \mu\text{m}$ corresponds to 16 accumulated laser pulses per area. $A_{\text{spot}} = \pi \cdot d_x \cdot d_y$ describes the area of the interfering laser beams and N the number of consecutive scans. In all experiments, the repetition rate remained constant, resulting in pulse energies E_p of $612 \mu\text{J}$, with calculated cumulated laser fluence values Φ_{cum} spanning from 4.1 to 122.3 J cm^{-2} .

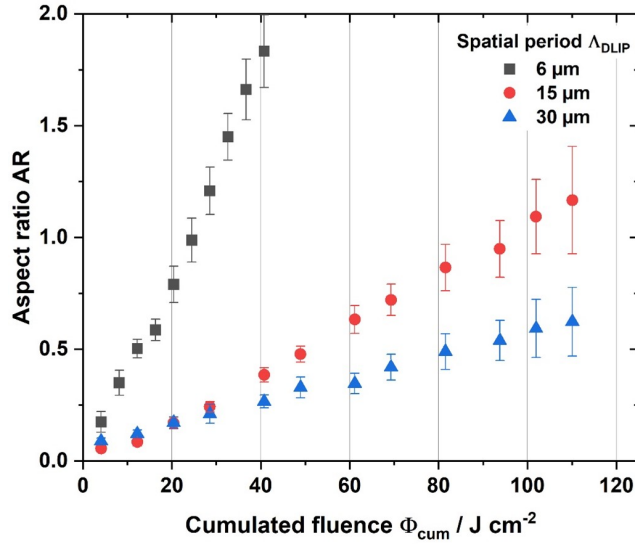


Figure S1: Aspect ratio AR of resulting line-like DLIP structures in dependency of the cumulated laser fluence Φ_{cum} for spatial periods Λ of 6, 15 and $30 \mu\text{m}$ fabricated with a single pulse fluence Φ_{sp} of 0.25 J cm^{-2} and a pulse-to-pulse distance PtP of $5 \mu\text{m}$ for different number of scans N .

The generated AR for the single-line experiments (without laser beam hatching) in relation to the applied cumulated fluences are presented in Fig. S1. For this analysis, only the central area of the ablated zone, corresponding to the peak fluence of the Gaussian laser spot, was considered. Across all spatial periods Λ , an increase in cumulative laser fluence resulted in a linear rise of AR for the DLIP line-like features.

The steepest increase in the AR curve was observed for the smallest spatial period of $6 \mu\text{m}$, while larger structure periods led to a continuous flattening of the aspect ratio curves. This flattening could be attributed to the enlargement of the maxima regions within the interference profile, resulting in lower ablation rates. Therefore, it can be concluded that higher energy densities (cumulative fluences) are necessary to achieve higher aspect ratios for larger structure periods. For the $6 \mu\text{m}$ period, the highest AR of 1.8 was achieved, with a greater volume of material vaporized due to the laser-material interaction compared to other structure periods. Maximum aspect ratios of 1.2 and 0.6 were reached for structure periods of $15 \mu\text{m}$ and $30 \mu\text{m}$, respectively.

Based on these results, nickel electrode areas of $25 \text{ mm} \times 10 \text{ mm}$ were equipped with line-like DLIP features aiming to generate aspect ratios of 0.33, 0.67 and 1.0 for all mentioned spatial

periods. It should be noted that an aspect ratio of 1.0 was not achieved for the structure period of $30\ \mu\text{m}$. The reason was the significant bending of the nickel foils caused by high thermal stresses during processing with elevated cumulative energy densities. As a result of this bending, the alignment of the individual laser lines could no longer be maintained, leading to partial destruction of the microstructure.

S3 Working electrode holder

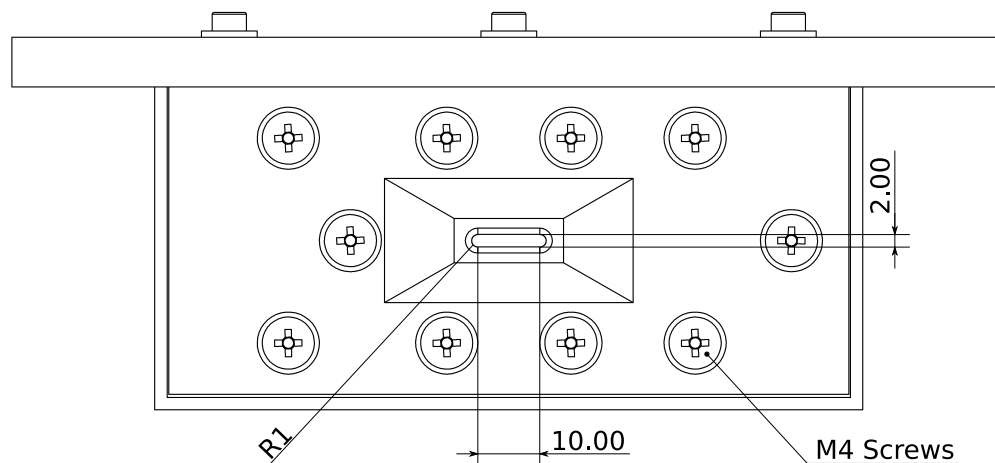


Figure S2: Drawing of the working electrode holder with dimensions of the open area.

S4 Image processing

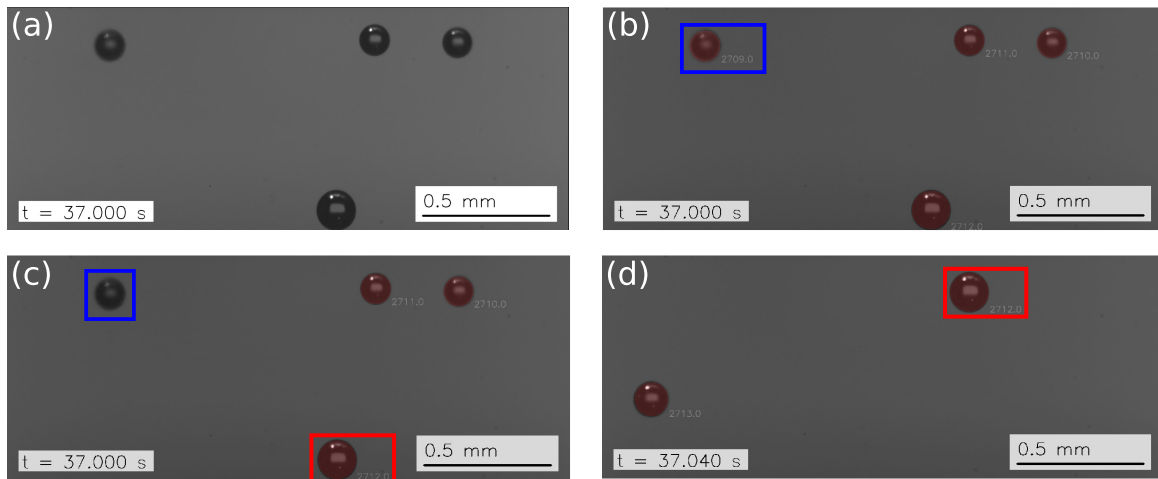


Figure S3: Procedure of image processing of sideview images: (a) Raw image, where (b) all bubble-like objects are segmented and linked (e.g. tracked bubble highlighted in red rectangle in (c-d)) using stardist and trackpy, respectively. Afterwards, by calculating the size-normalized variance of the bubble image Laplacian ($\text{Var}(\Delta) \cdot d_B$) blurred bubbles, like the highlighted bubble in the blue rectangle can be excluded.

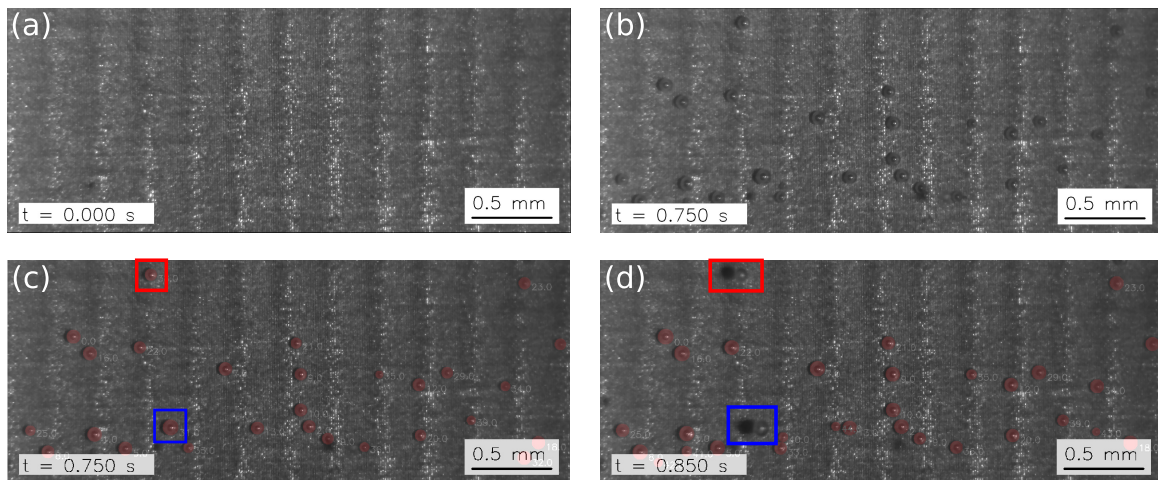


Figure S4: Procedure of image processing of topview images: (a) Clean electrode surface at beginning of experiment and (b) evolving O_2 -bubbles after applying j . (c-d) Segmented and linked bubbles sitting on electrode using stardist and trackpy, respectively. The highlighted bubbles show the distinction between bubble sitting on the electrode and detached, rising bubble with a shadow cast on the electrode surface.

S5 Electrode surface

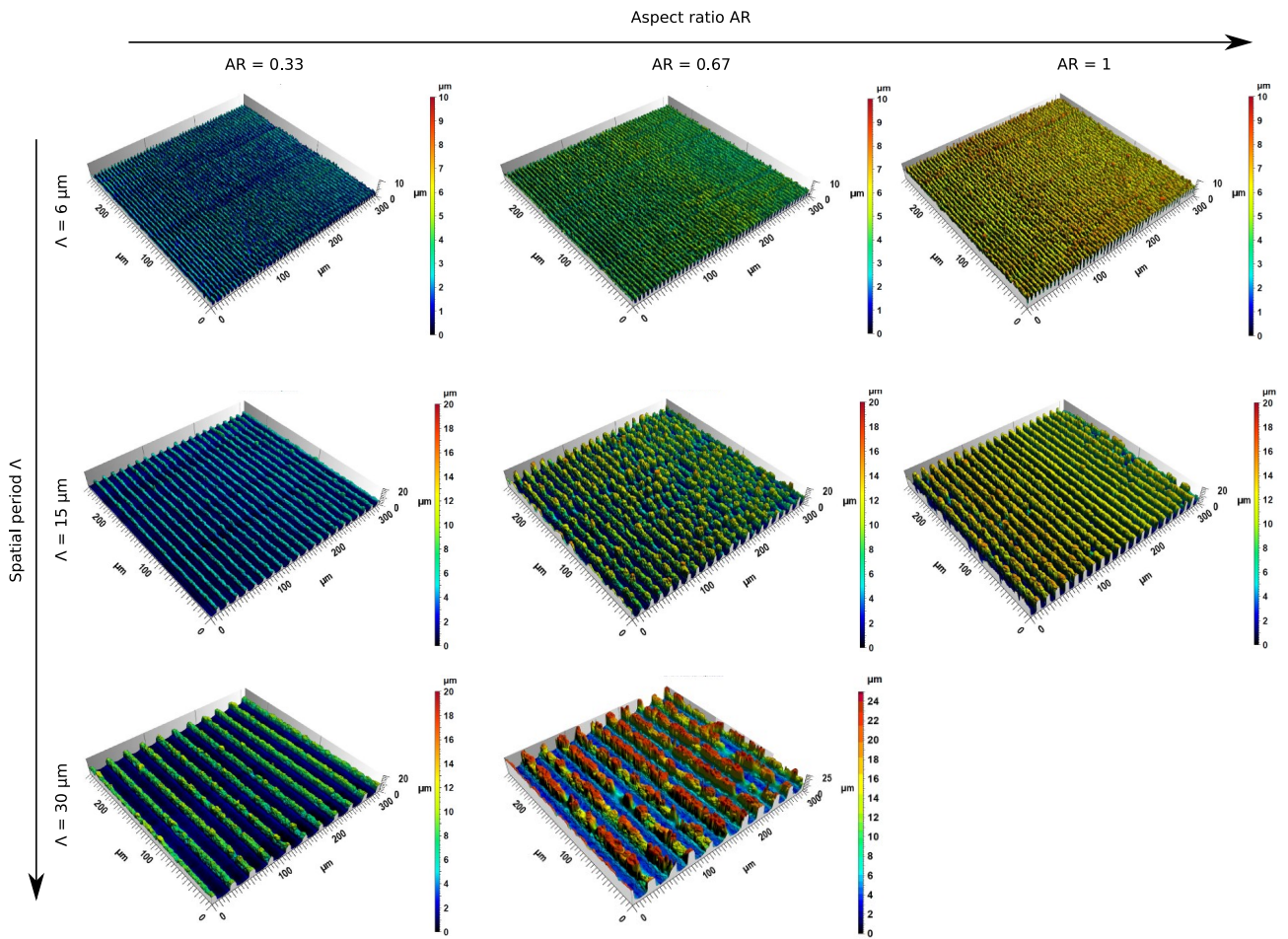


Figure S5: 3D confocal images of all DLIP line-like structures.

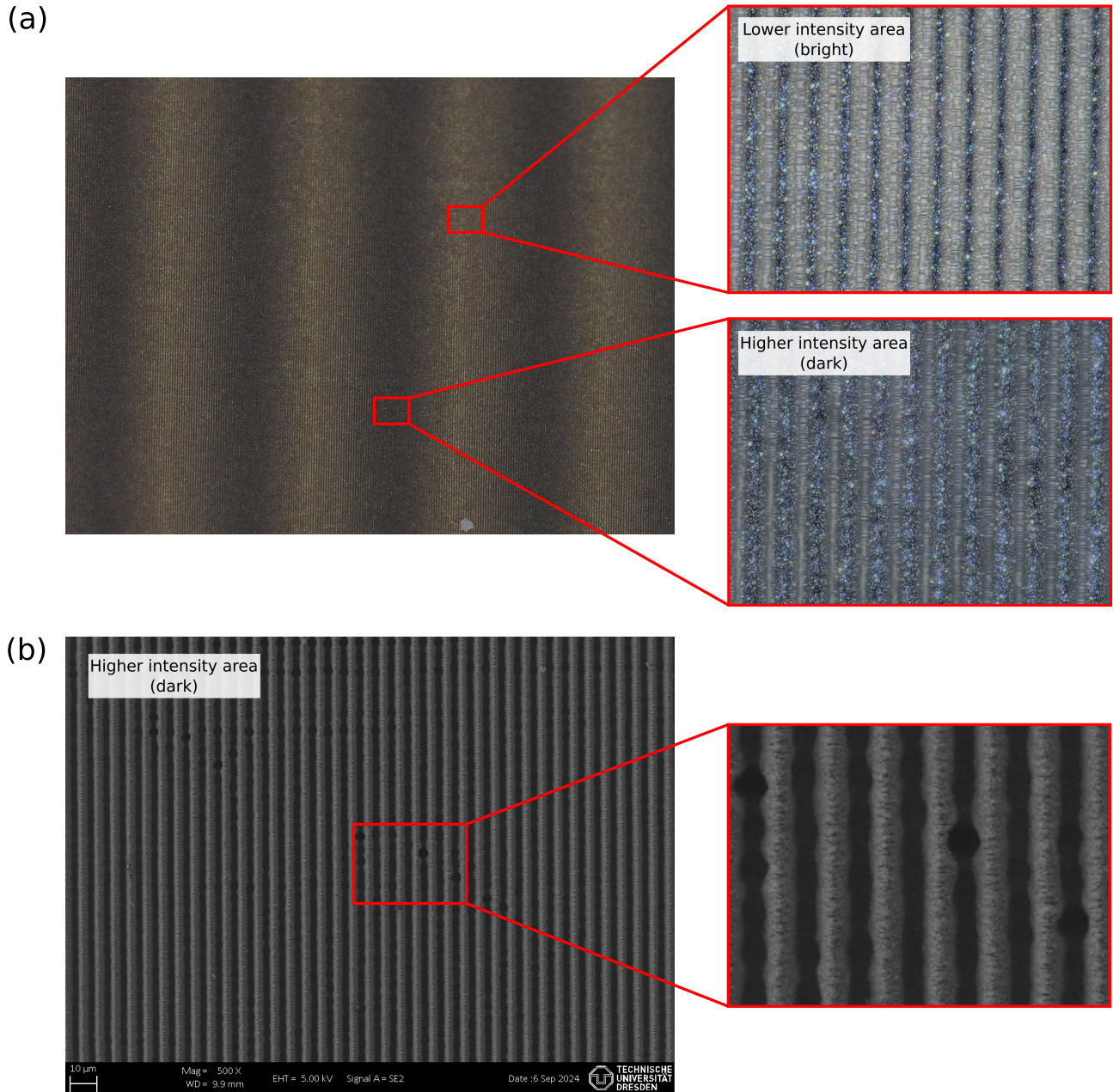


Figure S6: (a) Images of electrode #4 ($\Lambda = 6 \mu\text{m}$ and $AR = 1$) taken with a Keyence VHX Digital Microscope showing a more shallow profile for the brighter area. (b) SEM image of the higher intensity (dark) area of electrode #4 showing microholes in the maxima region of the interference pattern, which are not present in the lower intensity area.

S6 Wetting of electrodes

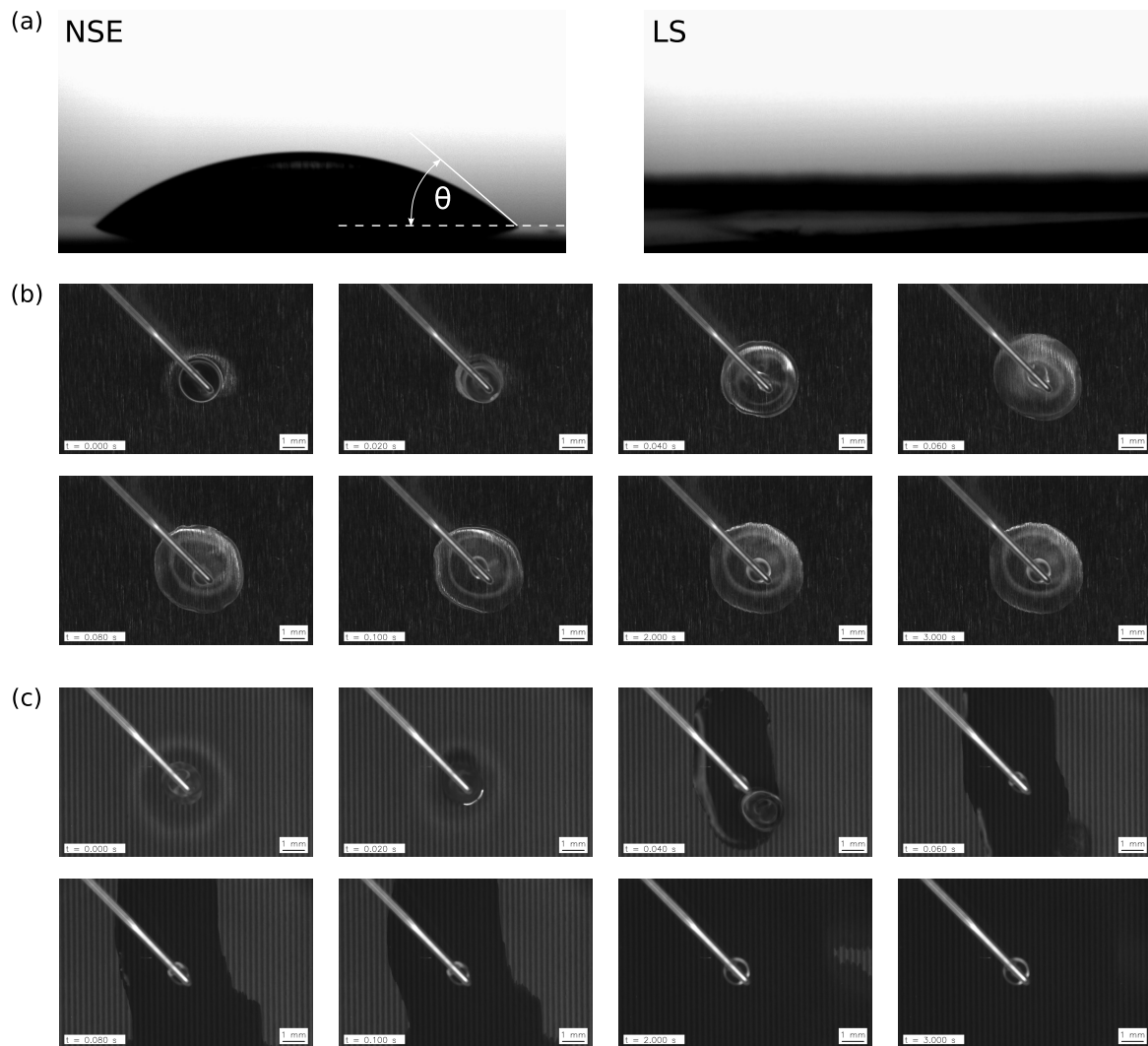


Figure S7: (a) Contact angle measurement of electrodes with highlighted $\theta_{\text{NSE}} \approx 38.5^\circ$ and the non-visible droplet on the DLIP-structured electrode due to superhydrophilic surface. Wetting behaviour of (b) non-structured and (c) laser-structured Ni-foil showing superhydrophilic wetting of laser-structured surface by applying a droplet of ≈ 0.2 ml of DI water on the surface with a 0.4 mm needle and the droplet spreads within less than 3 s across entire surface.

S7 Electrochemical characterization of electrodes

S7.1 Measurement of double-layer capacitance

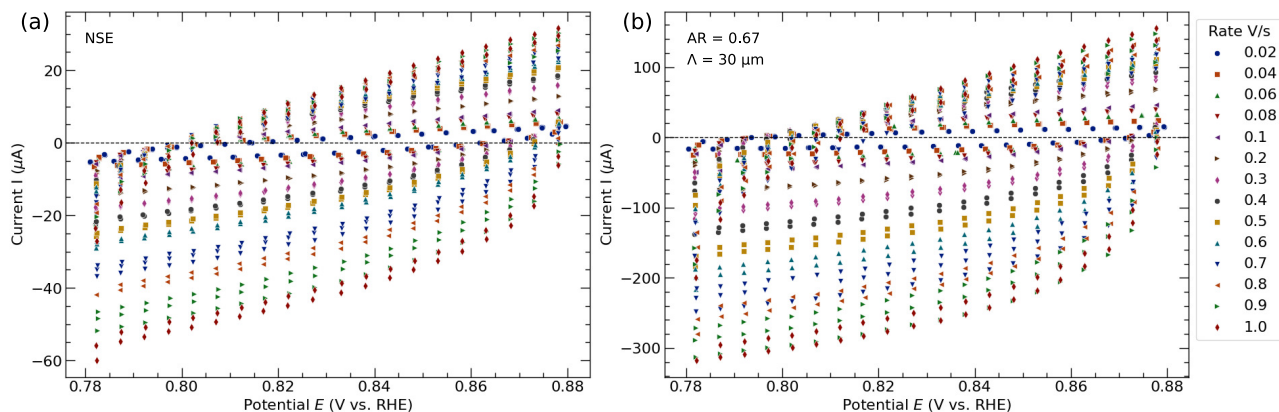


Figure S8: CVs at different scan rates ν for (a) NSE and (b) DLIP-structured electrode.

S7.2 Measurement of onset potential

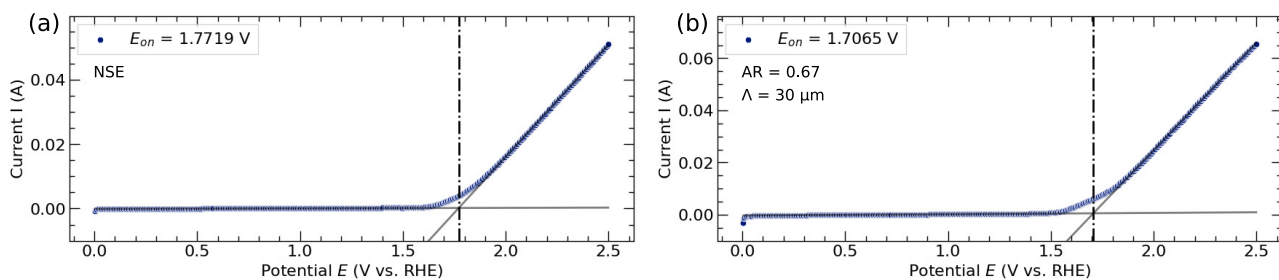


Figure S9: LSVs for (a) NSE and (b) DLIP-structured electrode with fitted tangents to calculate E_{on} .

S8 XPS Spectra

S8.1 Deconvolution and fitting of XPS Spectra

For the fitting of the detailed study on the influence of the LIPSS structures (dark/bright pattern) on the electrode surfaces, slightly different values of the binding energy were used for individual spectra. In these cases, the binding energy used is given in brackets.

The C 1s spectra for all samples were fitted with four components. First line centered at 285.0 eV arise from aliphatic carbon C-C, second line lies at 286.5 eV and indicate presence of C-O and/or C-N bonds, third line centered at 288.2 eV indicate presence of C=O and/or N-C=O bonds^{80,81}, and fourth line at 289.3 eV indicate presence of O-C=O and or CO₃²⁻ type compounds⁸⁰.

The N 1s spectra were fitted with up to three lines: first centered at 398.3 eV indicate presence of N=C type bonds, second line at 400.1 eV originates from central three-coordinated nitrogen N-C₃ and/or amine type groups and third line positioned at 402.6 eV which comes from NH₄⁺ type ions presence^{80,82}. For the LIPSS study only a single line centered at 400.0 eV was used for fitting the N 1s spectra, indicating the presence of N-C=O and/or C-NH type groups^{80,82}.

The O 1s spectra are similar for all samples and were fitted using three lines, with first line centered at 529.8 eV (529.5 eV) which indicates presence of metal oxide (O-Ni), second line at 531.5 eV (531.2 eV) indicates presence of defective oxygen in metal oxides and/or O=C and/or O-Si type bonds and/or CO₃²⁻ groups, and the last line found at 532.2 eV (532.6 eV) which can originate either from O-H and/or C-O type bonds and/or adsorbed H₂O^{80,83,84}.

The P 2p spectra were fitted with doublet structure (p_{3/2} - p_{1/2} doublet separation equals 0.84 eV) with main 2p_{3/2} line centered at 133.2 eV which indicates presence of P⁵⁺ oxidation state like in PO₄³⁻⁸⁵.

For the LIPSS study instead of the P 2p spectra, the Si 2p spectra show two doublet structures (doublet separation p_{3/2} - p_{1/2} equals 0.6 eV) with first 2p_{3/2} line centered at 102.0 eV which indicate presence of C-Si-O type bonds like in silicones/siloxanes⁸⁵ and second 2p_{3/2} line centered at 103.7 eV which indicate presence of silica type compounds like in e.g. SiO₂^{84,85}.

The S 2p spectra were fitted with doublet structure (p_{3/2} - p_{1/2} doublet separation equals 1.16 eV) with main 2p_{3/2} line centered at 168.3 eV which indicate presence of SO₃²⁻ ions^{85,86}.

The spectra collected at Ni 2p_{3/2} region are similar for all samples where nickel was detected. Each spectrum was fitted with up to six lines. First asymmetric line centered at 852.3 eV indicate presence of metallic nickel whereas second line found at 853.8 eV indicate the Ni²⁺ in nickel oxide NiO and/or hydroxide⁸⁷⁻⁸⁹. The four lines within energy range of 855 - 866 eV are due to the multiplet splitting phenomena.

S8.2 XPS Spectra and surface composition

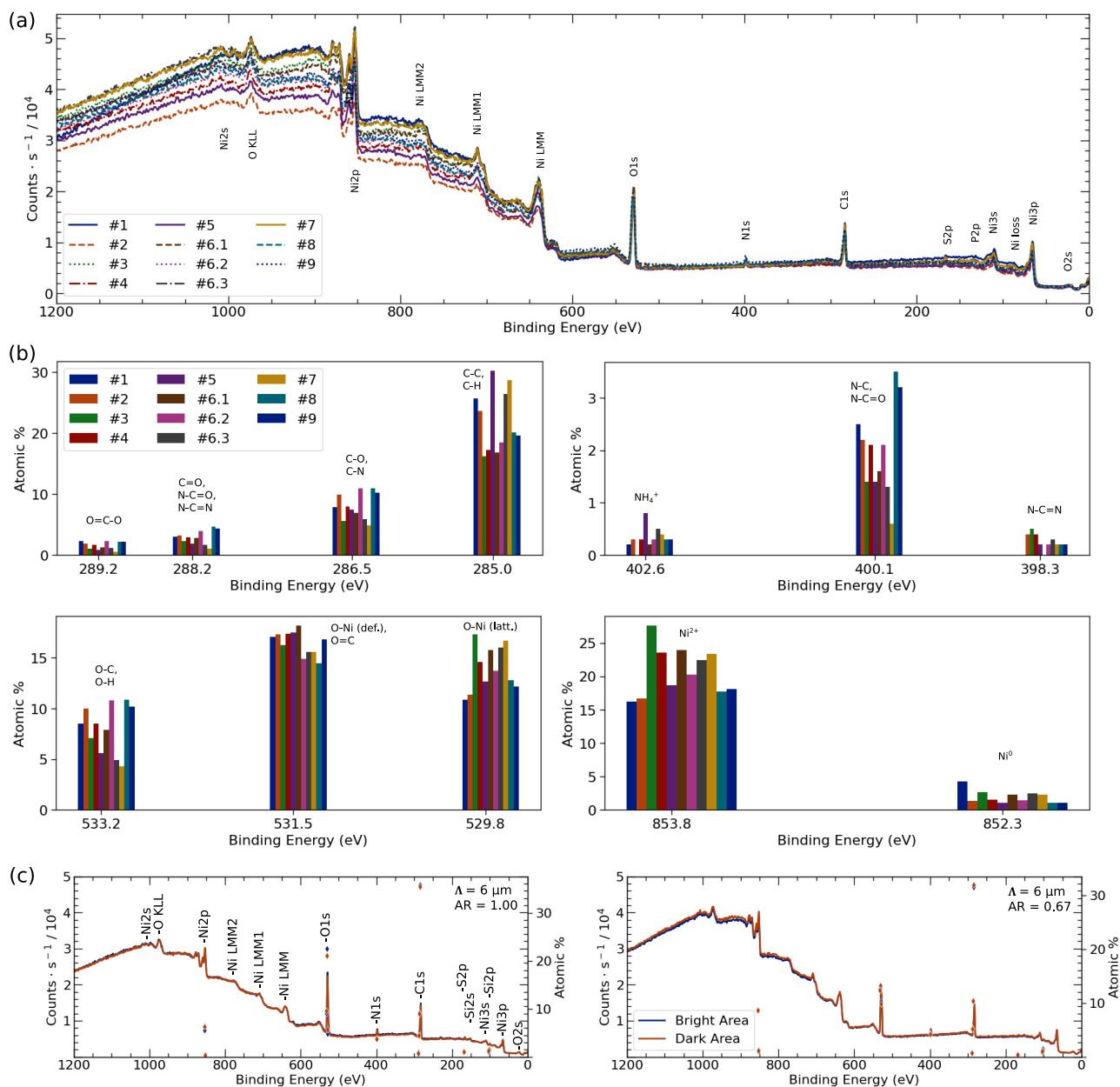


Figure S10: (a) Survey spectra of XPS measurements and (b) surface composition for the Elements C, N, O and Ni for all studied electrodes. (c) Survey spectra of XPS measurements and surface composition inside and outside of *HD* (dark/bright pattern, see Fig. S6) of the two electrodes for which linear patterned bubble nucleation could be observed.

Table S2: Surface composition (in atomic %) determined by fitting XPS spectra for all studied electrodes. The position of the 100 μm X-ray focus spot was chosen randomly on the electrode surface. Thus, no distinction is made between HIA and LIA.

Element	C			N			O			P	S	Ni		
BE (eV)	285.0	286.5	288.2	289.2	398.2	400.1	402.6	529.8	531.5	533.2	133.2	168.3	852.3	853.8
Groups,	C-C,	C-O,	C=O,			N-C			O-Ni(def.),	O-C,				
Ox. state	C-H	C-N	N-C=O	O=C-O	N-C=N	N-C=O	NH ₄ ⁺	O-Ni (latt.)	O=C	O-H	PO ₄ ³⁻	SO ₃ ²⁻	Ni ⁰	Ni ²⁺
			N-C=N											
#1	25.7	7.8	3.0	2.3	0.0	2.5	0.2	10.9	17.1	8.5	0.6	0.8	4.3	16.2
#2	23.6	9.9	3.2	1.9	0.4	2.2	0.3	11.4	17.3	10.0	0.7	1.1	1.3	16.7
#3	16.2	5.6	2.3	1.1	0.5	1.4	0.0	17.3	16.3	7.1	1.5	0.4	2.7	27.6
#4	17.2	8.0	2.9	1.7	0.4	2.1	0.3	14.6	17.4	8.5	1.2	0.6	1.5	23.5
#5	30.2	7.4	1.9	0.8	0.2	1.4	0.8	12.7	17.5	5.6	0.0	1.7	1.1	18.7
#6.1	16.8	6.9	2.8	1.3	0.0	1.6	0.2	15.8	18.2	7.9	1.9	0.5	2.3	23.9
#6.2	18.5	10.9	3.9	2.3	0.2	2.1	0.3	13.7	14.9	10.8	0.0	0.9	1.4	20.3
#6.3	26.4	5.9	1.7	1.2	0.3	1.3	0.5	16.0	15.6	4.9	0.0	1.5	2.5	22.4
#7	28.6	4.9	1.1	0.5	0.2	0.6	0.4	16.7	15.6	4.3	0.0	1.4	2.3	23.4
#8	20.1	10.9	4.7	2.2	0.2	3.5	0.3	12.8	14.5	10.9	0.7	0.7	1.1	17.7
#9	19.6	10.2	4.3	2.2	0.2	3.2	0.3	12.2	16.8	10.2	0.3	0.7	1.1	18.1

S9 Models of the multiple regression analysis

For all studied responses

- Double-layer capacitance (C_{dl}),
- Onset potential (E_{on}),
- Quasi-steady state potential (E_{SS}),
- Number of nucleation sites (n_{nucl}),
- Mode (d_m) and median (d_{50}) value of the bubble size distributions,

response surface models were derived using multiple regression analysis for a better understanding of the influence of these factors:

- Spatial period (Λ)
- Aspect ratio (AR)
- Current density (j)

The resulting surface plots of these models are shown in Fig. S11.

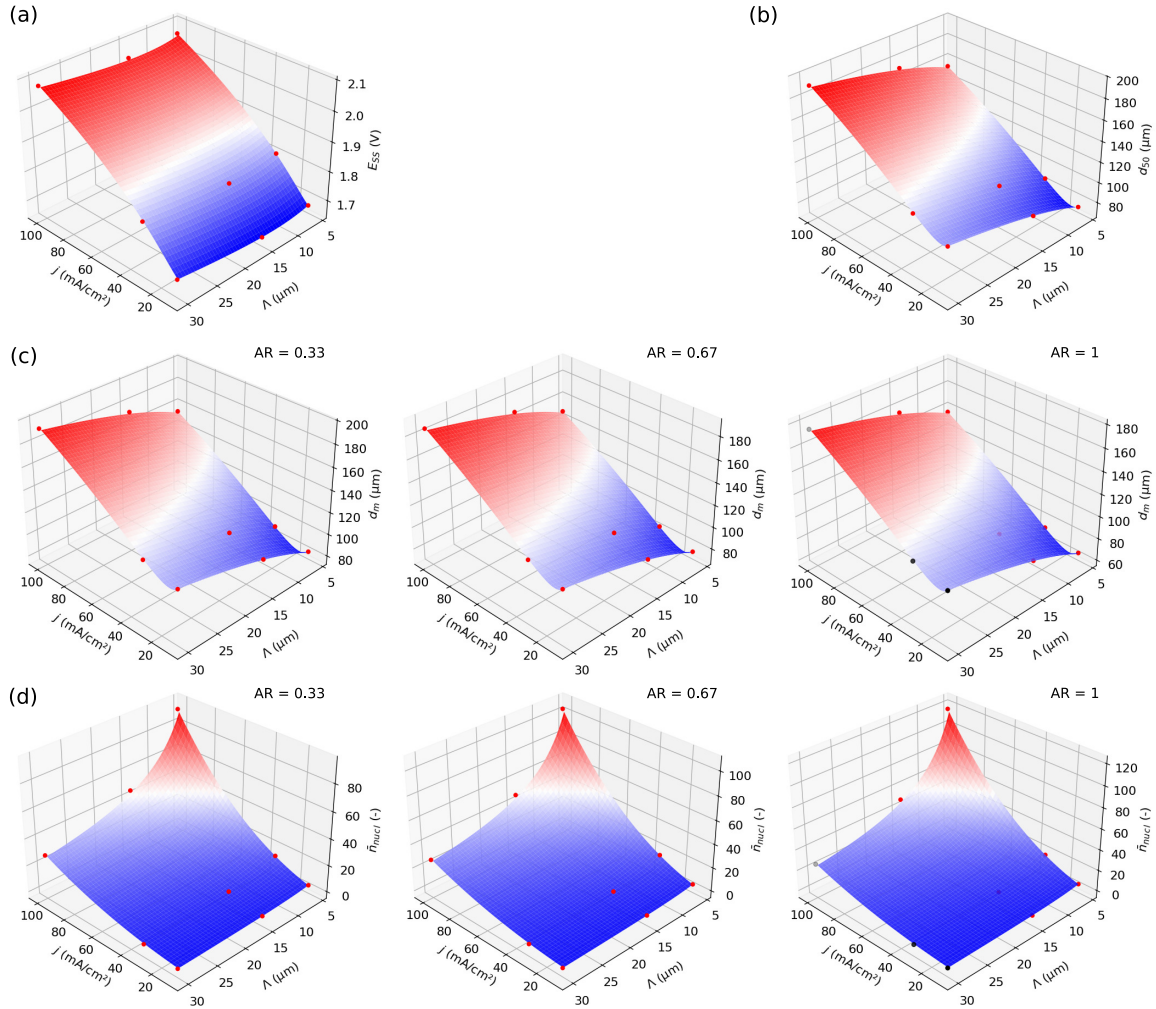


Figure S11: Surface plots of the determined models with highlighted measuring points of (a) E_{SS} , (b) d_{50} , (c) d_m and (d) \bar{n}_{nucl} . Measurement points at $AR = 1$ in (c) and (d) plotted in black mark the extrapolated data points of the non-existent electrode with $\Lambda = 30 \mu\text{m}$ and $AR = 1$.

S10 Error analysis of experiments

Table S3: Measurement noise (σ) of experiments calculated with the central and reference point of DoE for double-layer capacitance (C_{dl}), onset potential (E_{on}), quasi-steady state potential (E_{SS}), number of nucleation sites (n_{nucl}) and the mode (d_m) and median value (d_{50}) of the bubble size distributions

Parameter	Measurement point	
	Central point	Reference point
C_{dl}	4.6991 μF	1.7194 μF
E_{on}	0.0050 V	0.0215 V
E_{SS}	0.0244 V	-
n_{nucl}	3.5447	-
d_m	17.0762 μm	-
d_{50}	19.3189 μm	-

S11 Data and videos

Sample data sets with raw images, electrochemical measurement data, and results can be found at [10.14278/rodare.3064](https://doi.org/10.14278/rodare.3064). Due to the size of the complete data, the remaining image data can be made available upon request.

The provided characteristic videos are named after following scheme:

Perspective_Electrode_CurrentDensity \rightarrow E.g.: *Sideview_#1_NSE_100mAcm-2*